PAPER

Accelerator modes and anomalous diffusion in 3D volume-preserving maps

IOP Publishing | London Mathematical Society Nonlinearity

Nonlinearity 31 (2018) 5615–5642 https://doi.org/10.1088/1361-6544/aae69f

Accelerator modes and anomalous diffusion in 3D volume-preserving maps

James D Meiss[1], Narcís Miguel[2], Carles Simó[2] and Arturo Vieiro[2]

[1] Department of Applied Mathematics, University of Colorado Boulder, CO 80309-0526, United States of America
[2] Departament de Matemàtiques i Informàtica, Universitat de Barcelona (UB), Gran Via de les Corts Catalanes 585, 08007 Barcelona, Catalonia, Spain

E-mail: jdm@colorado.edu, narcis@maia.ub.es, carles@maia.ub.es and vieiro@maia.ub.es

Received 26 February 2018, revised 12 September 2018
Accepted for publication 8 October 2018
Published 15 November 2018

Recommended by Dr Tere M Seara

Abstract

Angle-action maps that have a periodicity in the action direction can have accelerator modes: orbits that are periodic when projected onto the torus, but that lift to unbounded orbits in an action variable. In this paper we construct a family of volume-preserving maps, with two angles and one action, that have accelerator modes created at Hopf-one (or saddle-center-Hopf) bifurcations. Near such a bifurcation we show that there is often a bubble of invariant tori. Computations of chaotic orbits near such a bubble show that the trapping times have an algebraic decay similar to that seen around stability islands in area-preserving maps. As in the 2D case, this gives rise to anomalous diffusive properties of the action in our 3D map.

Keywords: volume-preserving maps, accelerator modes, saddle-center Hopf, stability bubbles, anomalous diffusion
Mathematics Subject Classification numbers: 34C28, 37C05, 37G10, 60J60

(Some figures may appear in colour only in the online journal)

1. Introduction

In this work we consider real-analytic, volume-preserving maps (VPM) F on the cylinder $\mathbb{T}^d \times \mathbb{R}^l$, where $\mathbb{T}^d = \mathbb{S}^1 \times \overset{d}{\cdots} \times \mathbb{S}^1$, and $\mathbb{S}^1 = \mathbb{R}/\mathbb{Z}$. We think of the variables $(x, z) \in \mathbb{T}^d \times \mathbb{R}^l$ as being d-angles and l-actions, and call F an *angle-action* map. As an important, non-generic property, we will assume that F is the lift of a smooth map $\tilde{F}$ on the torus $\mathbb{T}^d \times \mathbb{T}^l$; that is, we assume there is a projection

$$\Pi : \mathbb{T}^d \times \mathbb{R}^l \to \mathbb{T}^{d+l}, \tag{1}$$

such that for each point in $\mathbb{T}^d \times \mathbb{R}^l$,

$$\tilde{F} \circ \Pi = \Pi \circ F. \tag{2}$$

We will simply take $\Pi(x, z) = (x, z \bmod 1)$: the unit modulus is applied to each action variable. Such maps may have special orbits, called *accelerator modes* that are unbounded orbits of F whose projections onto the torus become periodic orbits of $\tilde{F}$ [13, 14, 32, 50, 59]. The interest in such orbits is due to the fact that they can have a huge impact on the properties of chaotic orbits that are unbounded in the action direction—namely normal diffusion can become super, or anomalous, diffusion [34]. The way these diffusive properties change due to the presence of accelerator modes depends on the local structure of the phase space near the projected periodic orbit. And, as we will see, for finite-time simulations the statistics outside this local structure also plays a leading role.

Throughout this paper we label an orbit of F by subscripts, so that $(x_{t+1}, z_{t+1}) = F(x_t, z_t)$.

Accelerator modes have predominantly been studied for area-preserving maps defined on $\mathbb{S}^1 \times \mathbb{R}$ (i.e. for $d = l = 1$), as exemplified by Chirikov's standard map [13]

$$C_k : \mathbb{S}^1 \times \mathbb{R} \to \mathbb{S}^1 \times \mathbb{R}, \quad C_k : \begin{pmatrix} x \\ z \end{pmatrix} \mapsto \begin{pmatrix} x' \\ z' \end{pmatrix} = \begin{pmatrix} x + z' \\ z + k \sin(2\pi x) \end{pmatrix}. \tag{3}$$

As Chirikov showed, when the parameter $k = n \in \mathbb{N}_+ := \mathbb{N} \setminus \{0\}$ there are $2n$ accelerator-mode orbits

$$C_n(\tfrac{1}{4}, p) = (\tfrac{1}{4}, p + n), \quad C_n(\tfrac{3}{4}, q) = (\tfrac{3}{4}, q - n), \qquad p, q \in \mathbb{Z},$$

that project onto two fixed points of $\tilde{C}_n$ located at $\boldsymbol{P}_1 = (\frac{1}{4}, 0)$ and $\boldsymbol{P}_2 = (\frac{3}{4}, 0)$. When k is an integer these fixed points are parabolic. The unfolding of this bifurcation will be recalled in section 2.1. When $\kappa_n = k - n > 0$, is small, there appear islands of stability. Chaotic orbits outside these islands of stability may be trapped nearby for many iterations, a phenomena known as *stickiness* [31, 32]. In the map C_k this produces large excursions in the action variable z.

There has been some previous work on the existence and effects of accelerator modes for higher-dimensional symplectic maps. In [33] the authors report on the stickiness effects produced by the accelerator modes for the example of the four-dimensional Froeschlé map. A possible scenario leading to the creation of bubbles of stability in 4D has been investigated recently [4, 5]. However, as far as the authors are aware, accelerator modes in 3D VPM have not yet been studied. This is the goal of this paper. We remark that the mechanism for the creation of such bubbles in four-dimensional maps reported in [4, 5] is different than the one explained in this work. In particular in the present case the bubbles appear for a codimension-one set of values of the parameter while in the 4D example they require higher codimension.

The aim of this paper is to understand this phenomenon for three-dimensional VPM with two-angles and one-action. Such maps can be thought of as an intermediate case between

the area-preserving and four-dimensional symplectic cases, but they nevertheless have some distinctive geometrical and dynamical features. For example, the invariant tori that persist in the 3D case with two frequencies and one action have codimension one, while in the 4D symplectic case they would have codimension two. This can play an important role in the trapping statistics. Moreover, 3D VPM are interesting in themselves since they model periodically time-dependent velocity fields in incompressible fluid flows. Such flows have been studied both experimentally and in models, e.g. [22, 29, 47, 51, 52].

More concretely, in this paper we will:

1. *Construct a one-parameter family of VPM of the cylinder* $\mathbb{T}^2 \times \mathbb{R}$ *that has accelerator modes* (see section 3).
   We restrict ourselves to a family $\boldsymbol{F}_\varepsilon : \mathbb{T}^2 \times \mathbb{R} \to \mathbb{T}^2 \times \mathbb{R}$ of the form:
   $$\boldsymbol{F}_\varepsilon : \begin{pmatrix} x \\ y \\ z \end{pmatrix} \mapsto \begin{pmatrix} x' \\ y' \\ z' \end{pmatrix} = \begin{pmatrix} x + \Omega_1(z) \\ y + \Omega_2(z) \\ z \end{pmatrix} + \varepsilon \begin{pmatrix} h_1(x,y,z) \\ h_2(x,y,z) \\ h_3(x,y,z) \end{pmatrix}. \tag{4}$$
   The preservation of volume is imposed as $\det \boldsymbol{DF}_\varepsilon(x,y,z) \equiv 1$. The generalization from 2D to 3D will be done by constructing the family to mimic some features of Chirikov's map (3). Namely:
   (a) The parameter ε in (4) represents the deviation from integrability. For $\varepsilon = 0$ all orbits lie on 2D rotational invariant tori (RIT), $\{(x,y,z){:}z = z_0\}$, and the dynamics is simply a rigid rotation in the angles with rotation vector $\Omega(z_0) = (\Omega_1(z_0), \Omega_2(z_0))^\top$. For $\varepsilon > 0$, but small, $\boldsymbol{F}_\varepsilon$ is assumed to satisfy the hypotheses of the KAM-like theorems for volume-preserving maps [12, 58]. Hence there is a Cantor set of RIT.
   (b) Accelerator modes of $\boldsymbol{F}_\varepsilon$ are born at $\varepsilon = n \in \mathbb{N}_+$. These project to isolated fixed points of $\tilde{\boldsymbol{F}}_\varepsilon$.
   (c) When $0 < \varepsilon - n \ll 1$ there is a neighborhood of some of the accelerator modes that contains a bubble of trapped orbits that exhibit regular motion.
   The requirement (c) is mandatory since we are interested in accelerator modes that give rise to anomalous diffusion along the z coordinate. To ensure this, we will assume that the parameter $\kappa_n = \varepsilon - n$ unfolds a 'Hopf-one' or 'saddle-center-Hopf' bifurcation at the accelerator modes. This bifurcation, a discrete analogue of the Hopf-zero bifurcation for ODEs, corresponds to the creation of a fixed point with multipliers $\lambda_1 = 1$ and $\lambda_{2,3} = \mathrm{e}^{\pm 2\pi \mathrm{i}\omega}$ on the unit circle. The unfolding of this bifurcation gives rise to a pair of saddle-focus fixed points. There is a rich structure around the stability region where orbits may be trapped for a long time so that they affect the diffusion in the action variable. See section 2.4 for more discussion.
   The proposed family of maps $\boldsymbol{F}_\varepsilon$ seems to be the first studied example of VPM with accelerator modes.
2. *Study the effect of these accelerator modes on the diffusive properties of the action* (see section 4).
   We perform a numerical exploration based on long-term simulations of $\boldsymbol{F}_\varepsilon$ to study, on the one hand, the diffusive properties of the action, and on the other hand, the trapping statistics due to the passages near the stability region that appears in a vicinity of the accelerator modes. Here, by trapping statistics we mean the distribution of trapping times in a neighborhood of the accelerator-mode stability region. Our experiments suggest that

this behaves as t^{-b}, $b \in (2,3)$, which is consistent with the behavior observed in the area-preserving case. Furthermore, the action exhibits an anomalous, super-diffusive behavior.

This paper is organized as follows. In section 2 we recall some preliminary facts and set the problem in context by discussing the well-known area-preserving setting. We summarize some relevant facts on the Hopf-one bifurcation in the volume-preserving context. The rest of the paper is separated into two distinct parts according to the previous enumeration. In section 3 we construct a family of VPM with accelerator modes and study the scaling properties of the local dynamics. In section 4, we numerically study the diffusive properties and trapping statistics due to these accelerator modes for an example. In section 5 we discuss these results, taking into account geometrical and statistical facts. Finally, in section 6 we summarize our results and propose new lines of research that emerge from this study.

2. Preliminaries

In this section we introduce the main ideas on which this paper is based. In section 2.1 we review well-known facts about the accelerator modes of Chirikov's standard map: the mechanism of their creation, their local dynamics, and their effect on the action diffusion due to stickiness. This map serves as inspiration for the construction of our main model. In section 2.2 we generalize the concept of accelerator mode to higher-dimensional maps. In section 2.3 we define a VPM that can possess accelerator modes as a composition of simple shears. We finish this preliminary section by reviewing some facts on the Hopf-one bifurcation in volume-preserving maps in section 2.4. This is a mechanism that can create a region of stable motion in a vicinity of an accelerator mode.

2.1. Accelerator modes in area-preserving maps

One of the most studied area-preserving models with accelerator modes is Chirikov's standard map C_k (3) [13]. This map has three properties that we will generalize to higher dimensions.

1. *Accelerator modes*. As we noted in section 1, the backward and forward orbits of the points $P_1 = (\frac{1}{4}, 0)$ and $P_2 = (\frac{3}{4}, 0)$ are unbounded under C_n for $n \in \mathbb{N}_+$. These points are unstable, parabolic fixed points of the projection $\tilde{C}_n$, and their properties are equivalent under a reflection symmetry of the map. The parameter $\kappa_n = k - n$ unfolds a saddle-center bifurcation at P_1 (resp. P_2) giving rise to an elliptic fixed point $P_{1,e}$ and a hyperbolic fixed point $P_{1,h}$ (resp. $P_{2,e}$ and $P_{2,h}$) of $\tilde{C}_{n+\kappa_n}$. The positions of these fixed points depend on κ_n, but, to simplify the notation, we do not make this explicit. These four fixed points are projections of accelerator modes of C_k.
2. *Stability islands around elliptic accelerator modes and limit local dynamics.* When $0 < \kappa_n \ll 1$, islands of stability appear around $P_{1,e}$ and $P_{2,e}$. The area of these islands decreases with n as $1/n^2 + \mathcal{O}(n^{-6})$. The orbits $P_{1,e}$ and $P_{2,e}$ undergo a period-doubling bifurcation at $k = n + 2/(n\pi^2) + \mathcal{O}(n^{-3})$. Chirikov and Izraelev [14] showed that these scalings hold for a larger class of maps (where the force $\sin(2\pi x)$ in (3) is generalized to an odd periodic function of x). In [45] it was proved that the leading terms of the suitably scaled Taylor expansions of C_n around the accelerator modes could be written as the quadratic area- and orientation-preserving Hénon map (which we just call the Hénon map from now on) in Karney's form [32]

$$H_\kappa : \begin{pmatrix} \xi \\ \eta \end{pmatrix} \mapsto \begin{pmatrix} \xi' \\ \eta' \end{pmatrix} = \begin{pmatrix} \xi + \eta' \\ \eta + \kappa - 2\pi^2 \xi^2 \end{pmatrix}. \tag{5}$$

The corrections to this map are $\mathcal{O}(n^{-2})$ in each variable. Hence the Hénon map becomes asymptotically accurate as $n \to \infty$. Furthermore, the coefficients of the $\mathcal{O}(n^{-2})$ corrections are small [46], so that even when $n = 1$, the Hénon map is a fairly good approximation.

3. *Statistics of chaotic orbits in the presence of accelerator modes*. The stability islands around the accelerator modes are responsible for the anomalous transport of the action of $C_{n+\kappa_n}$. There are two interconnected problems of interest in this situation. Let us restrict ourselves to the island around $P_{1,e}$, though by the reflection symmetry, the following also applies to the island around $P_{2,e}$.

   (a) *Trapping statistics around stability islands*. Let $\mathcal{K}$ be a compact subset of the phase space that contains the stability island around $P_{1,e}$ for $\tilde{C}_k$. Initial conditions in $\mathcal{K}$ that are not confined by an invariant curve of the stability island or any of its satellites will escape from $\mathcal{K}$, but have a trapping probability that decays asymptotically as $t^{-\gamma}$, where $\gamma \in (1, 2)$ [17, 18, 28, 31, 32, 42, 41, 46, 55, 59]. Equivalently, the density of the exit-time distribution $\mathcal{P}_k(t)$, the probability that an orbit leaves $\mathcal{K}$ after exactly t iterates [40], decays as

   $$\mathcal{P}_k(t) \sim t^{-b}, \qquad b \in (2, 3), \tag{6}$$

   where $b = 1 + \gamma$ and $\sim$ denotes asymptotic behavior as $t \to \infty$. The numerical simulations—for finite times—show that b depends on k. Note that the probability density $\mathcal{P}_k(t)$ has bounded average but all higher-order moments are unbounded.

   (b) *Anomalous diffusion of the action*. The action diffusion is computed from the standard deviation $\sigma_T(k)$ of the action z after T iterates over an ensemble of orbits that are not confined in stability islands. Without accelerator modes, one expects [34]

   $$\sigma_T(k) \sim \sqrt{T},$$

   but when there is an elliptic accelerator mode, for example, when $\kappa_n \in (0, 2/(n\pi^2) + \mathcal{O}(n^{-3}))$, one observes super-diffusion:

   $$\sigma_T(k) \sim T^\chi, \quad \chi > \frac{1}{2}. \tag{7}$$

   Again, it is observed that the exponent χ depends on k in a complicated way.

The dependence of the exponents b and χ on k—for finite time simulations—is primarily due to the structure of the invariant sets (Cantori, satellite islands, etc) surrounding the main accelerator-mode island [42]. The variation of the exponents is most prominent just after the breakdown of an outermost invariant curve that had confined a large region of chaos. The corresponding values of κ_n where larger variations are expected are related to the breakdown of the invariant curves around elliptic periodic islands of moderate period, as can be seen in the Hénon map [45]. Even though this geometrical fact is well known, and forms the basis for most of the models of trapping statistics [2, 3, 18, 42, 54], it is still not completely understood theoretically and requires extensive numerical explorations for confirmation. We refer to [15, 16, 46, 59] for dedicated numerical explorations focusing on concrete Cantori with a prescribed rotation number.

It is natural to think that the exponents in $\sigma_T(k)$ and $\mathcal{P}_k(t)$ are related. Under some simplifying assumptions, it has been shown that $2\chi + b = 4$ [31]. This was also later derived in [24, 30, 57, 60, 61], see the review [1] and references therein. A similar result, obtained in [46], shows that $\sigma_T(k)$ is bounded from below by $T^{2-(b+1/b)/2}$ for large enough T.

2.2. Accelerator modes for higher-dimensional maps

As in section 1, let $F : (x, z) \mapsto (x', z')$ be a volume-preserving map of $\mathbb{T}^d \times \mathbb{R}^l$ that smoothly projects to a map $\tilde{F}$ on the torus $\mathbb{T}^d \times \mathbb{T}^l$, as defined by (2).

As in the area-preserving case, an accelerator mode of F is an orbit with unbounded action that projects to a periodic orbit of $\tilde{F}$, due to the periodicity of the map in the action direction. This implies that the action increases linearly under iteration of F.

Definition 1. The orbit of a point (x, z) under F is an accelerator mode if there exist $q \geqslant 1$ and $n \in \mathbb{Z}^l \setminus \{0\}$ such that $F^q(x,z) = (x,z + n)$.

Note that the projection of an accelerator mode is a q-periodic orbit of $\tilde{F}$. In section 2.3 we present a simple way to generate VPM on the cylinder $\mathbb{T}^2 \times \mathbb{R}$ with accelerator modes. We are mainly interested in those accelerator modes that project onto fixed points of $\tilde{F}$, i.e. for $q = 1$. We refer to these kind of orbits as 'fixed point' accelerator modes, or simply FPAM.

2.3. Volume-preserving maps as compositions of shears

To ease the construction of volume-preserving maps, we will consider angle-action maps that are compositions of shears. Let S_i be a shear in the ith direction, that is, if $w = (x, z) \in \mathbb{T}^{d+l}$, then $S_i : \mathbb{T}^{d+l} \to \mathbb{R}^{d+l}$ is

$$S_i(w) = w + s_i(w)\,\hat{e}_i,$$

where $s_i : \mathbb{T}^{d+l} \to \mathbb{R}$ is a smooth function that is independent of the ith component, w_i, and $\hat{e}_i$ is the ith unit vector in the canonical basis of $\mathbb{R}^{d+l}$. Assuming that s_i projects to a smooth function on the circle $\mathbb{R}/\mathbb{Z}$, then S_i projects to a smooth, volume and orientation preserving map, $\tilde{S}_i$, on $\mathbb{T}^{d+l}$. Thus any composition $\tilde{F} = \tilde{S}_{i_1} \circ \tilde{S}_{i_2} \circ \ldots \circ \tilde{S}_{i_j}$ with arbitrary $j \geqslant 1$ and $i_1, i_2, \ldots, i_j \in \{1, 2, \ldots, d + l\}$ is a volume-preserving map on the $d + l$-torus.

In this paper, we are interested in the dynamics of a volume-preserving map with two angles $(x_1, x_2) = (x, y) \in \mathbb{T}^2$ and one action $z \in \mathbb{R}$, and we will use three shears, one in each direction:

$$S_1 : \begin{pmatrix} x \\ y \\ z \end{pmatrix} \mapsto \begin{pmatrix} x + s_1(y,z) \\ y \\ z \end{pmatrix}, \quad S_2 : \begin{pmatrix} x \\ y \\ z \end{pmatrix} \mapsto \begin{pmatrix} x \\ y + s_2(x,z) \\ z \end{pmatrix}, \quad S_3 : \begin{pmatrix} x \\ y \\ z \end{pmatrix} \mapsto \begin{pmatrix} x \\ y \\ z + s_3(x,y) \end{pmatrix}.$$

There are two sets of conjugate maps formed by composition of these three shears in some order, but the families are equivalent under permutations of the labels. To fix ideas, we let $\tilde{F} = \tilde{S}_2 \circ \tilde{S}_1 \circ \tilde{S}_3$,

$$\tilde{F} : \begin{pmatrix} x \\ y \\ z \end{pmatrix} \mapsto \begin{pmatrix} x' \\ y' \\ z' \end{pmatrix} = \begin{pmatrix} x + s_1(y,z') \\ y + s_2(x',z') \\ z + s_3(x,y) \end{pmatrix} \mod 1. \tag{8}$$

We will assume that the functions s_i are either periodic or degree-one functions of their arguments. In this case periodic orbits of $\tilde{F}$ on $\mathbb{T}^3$ may not be periodic orbits of F, the lift to $\mathbb{T}^2 \times \mathbb{R}$: the lifted z variable may increase or decrease by an integer amount in q iterates for suitable (x, y). Thus for an FPAM, there must exist points (x_0, y_0, z_0) such that $F(x_0, y_0, z_0) = (x_0, y_0, z_0 + n)$ for some nonzero integer n.

The inverse of the map (8) is simply given by $\tilde{F}_\varepsilon^{-1} = S_3^{-1} \circ S_1^{-1} \circ S_2^{-1}$, where the three inverses S_j^{-1}, $j = 1, 2, 3$ are obtained by simply changing the sign of the functions s_i.

In section 3.1 we will obtain a one-parameter family of maps F_ε, by letting $s_3(x, y) \to \varepsilon s_3(x, y)$. The existence of an FPAM will then depend upon the parameter ε.

2.4. The Hopf-one bifurcation in volume-preserving maps

Suppose that the map (8) has an accelerator mode. In this section we will add extra conditions on F to ensure that the corresponding periodic orbit of $\tilde{F}$ has a neighborhood of stable motion. For area-preserving maps, stable motion around accelerator modes is generated by a saddle-center bifurcation, recall section 2.1. A generalization of this mechanism to VPM is the codimension-two, *Hopf-one* or saddle-center-Hopf bifurcation [19, 20]. This bifurcation is the discrete-time, volume-preserving version of a bifurcation that has been variously called the Hopf-zero, fold-Hopf or Gavrilov–Guckenheimer bifurcation [27].

To guarantee that there is a stability region near an accelerator mode that is born from a Hopf-one bifurcation, we will require that the leading terms of the Taylor expansion give a map that is locally conjugate, using a suitable scaling, to a map, $M_{\varphi,a} : \mathbb{R}^3 \to \mathbb{R}^3$, of the form

$$M_{\varphi,a} : \begin{pmatrix} u \\ v \\ w \end{pmatrix} \mapsto \begin{pmatrix} u' \\ v' \\ w' \end{pmatrix} = \begin{pmatrix} u + \varphi v \\ v + \varphi w' \\ w + \varphi \left(1 - u^2 - a v\right) \end{pmatrix}, \tag{9}$$

for suitable values of the parameters φ and a. This map can be regarded as a 3D analogue of the Hénon map (5) since (a) it is a quadratic truncation of the unfolding of the normal form near a triple-one multiplier [20], (b) its inverse is also a quadratic volume-preserving map [35], and (c) it appears as a truncation of the return map near a homoclinic quadratic tangency [25].

The map (9) is a discretization of the well-known Michelson ODEs [43]

$$\frac{\mathrm{d}u}{\mathrm{d}t} = v, \quad \frac{\mathrm{d}v}{\mathrm{d}t} = w, \quad \frac{\mathrm{d}w}{\mathrm{d}t} = 1 - u^2 - a v, \qquad a > 0, \tag{10}$$

that appear in travelling wave solutions of the Kuramoto–Sivashinsky PDE. The flow of (10) has an 'integrable' limit for $a \to \infty$. To see this, it is convenient to introduce the scaling $u = \xi$, $v = \sqrt{a}\eta$, $w = a\zeta$, $t = \tau/\sqrt{a}$. Then (10) reads

$$\frac{\mathrm{d}\xi}{\mathrm{d}\tau} = \eta, \quad \frac{\mathrm{d}\eta}{\mathrm{d}\tau} = \zeta, \quad \frac{\mathrm{d}\zeta}{\mathrm{d}\tau} = \varepsilon(1 - \xi^2) - \eta, \tag{11}$$

where $\varepsilon = a^{-3/2}$. The system (11) has an equilibrium at $(-1, 0, 0)$ with eigenvalues $2\varepsilon + \mathcal{O}(\varepsilon^3)$ and $\pm i - \varepsilon + \mathcal{O}(\varepsilon^2)$, and an equilibrium at $(1, 0, 0)$ with eigenvalues $-2\varepsilon + \mathcal{O}(\varepsilon^3)$ and $\pm i + \varepsilon + \mathcal{O}(\varepsilon^2)$.

When a grows, and therefore ε decreases, the measure of the set of bounded orbits of (11) also grows. To study this limit, introduce the variable $s = \xi + \zeta$ and cylindrical coordinates (R, θ) with $\eta = R\cos\theta$ and $\zeta = R\sin\theta$. Now when $\varepsilon \ll 1$ and R is bounded from below, the

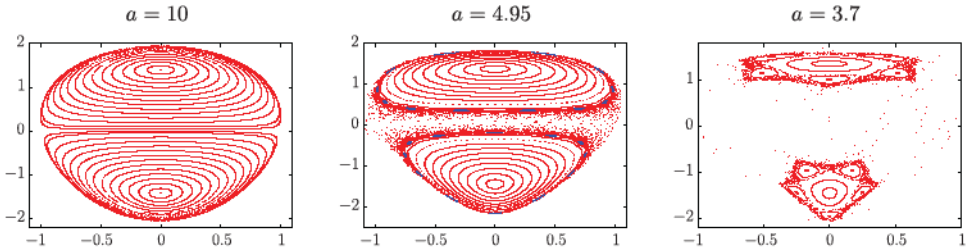

Figure 1. Slices $|\zeta| < \delta$ of trajectories of the map (9), in the (ξ, η, ζ) coordinates of (11), showing the rectangle $-1 < \xi < 1, -2 < \eta < 2$. The parameters are $a = 10$, $\varphi = 0.1$, $\delta = 0.001$ (left), $a = 4.95$, $\varphi = 0.01$, $\delta = 0.001$ (middle), and $a = 3.7$, $\varphi = 0.001$, $\delta = 0.0001$ (right).

dynamics is fast in θ, namely $\dot\theta = -1 + \mathcal{O}(\varepsilon/R)$, while it is slow in s. After averaging over the fast angle, R becomes also slow and the system reads

$$\frac{ds}{d\tau} = \varepsilon\left(1 - s^2 - \frac{R^2}{2}\right), \qquad \frac{dR}{d\tau} = \varepsilon R s.$$

This system has the integral

$$h = R^2\left(1 - s^2 - \frac{R^2}{4}\right). \tag{12}$$

The domain of interest is $h \in [0, 1]$. The level $h = 0$ contains the two saddle-foci of (11) at $(s, R) = (\pm 1, 0)$. The level $h = 1$ corresponds to an elliptic equilibrium $(s, R) = (0, \sqrt{2})$, which approximates, as $\varepsilon \to 0$, the intersection of an elliptic periodic orbit of (11) with the Poincaré section $\{\zeta = 0\}$. The level sets $h \in (0, 1)$ are close to invariant circles on the Poincaré section of the flow of (11) [21]. These correspond to 2D invariant tori of (11). When $\varepsilon \ll 1$, the ratio of the two frequencies on the invariant tori is large.

More generally, the system (11) has two equilibria that are saddle-foci: $Q^l = (-1, 0, 0)$ and $Q^r = (1, 0, 0)$ which have 1D invariant manifolds $W^u(Q^l)$ and $W^s(Q^r)$ that nearly coincide as $\varepsilon \to 0$. As ε tends to zero, the 2D invariant manifolds $W^s(Q^l)$ and $W^u(Q^r)$ approach a spherical shell, that we refer to as the *bubble* [9–11, 56]. The bubble encloses a family of nested tori around a normally elliptic invariant circle (see e.g. figure 1(a)) when ε is small enough. If $\varepsilon > 0$ (11) is not integrable and the 1D and 2D invariant manifolds no longer coincide [6–8, 21]. See [21] for a detailed numerical study of the region of bounded motion of (10)[3].

The quadratic map (9) is also not integrable. Fixing $a > 0$, the points Q^l and Q^r are saddle-foci when φ small enough [20]. This occurs approximately when $a\varphi^2 \in (0, 4)$. More precisely, if $\varphi < \frac{1}{2}$ it is sufficient to have $a\varphi^2 < 3.87$ and if $\varphi < \frac{1}{4}$ it is sufficient to have $a\varphi^2 < 3.98$. For these values of the parameters some of the bubble structure of the flow is preserved. Namely, the 2D invariant manifolds of Q^l and Q^r (which do not coincide), bound a Cantor family of invariant tori that enclose, for most values of the parameters φ and a, an elliptic invariant circle [20].

When $\varphi \ll 1$, the dynamics of (9) limits on that of the ODEs (10). In figure 1 we show, in the (ξ, η, ζ) coordinates of (11), the points on some orbits which start in the slice $|\zeta| < \delta \ll 1$. The orbits shown in the three panels pass through this slice, moving 'up', $\zeta' > \zeta$, when $\eta \lesssim 0$ and 'down', $\zeta' < \zeta$, if $\eta \gtrsim 0$. The boundary between the orbits going 'up' and 'down' is

[3] A movie of the evolution of the flow with a is at www.maia.ub.es/dsg/moviehsn

$\eta = \varepsilon(1-\xi^2)$. For the leftmost panel, where $a = 10$, the set of bounded orbits resembles that of the integrable case discussed above: at $\xi \approx 0$ and $\eta \approx \pm\sqrt{2}$ we observe what seem to be two elliptic fixed points that are actually points on a transversally elliptic invariant circle. The nested invariant curves in the plot are slices through invariant tori surrounding this circle. For the center panel, where $a = 4.95$, one can also see satellite islands and several unbounded orbits that are temporarily trapped near the outermost torus. The blue points correspond to the intersection of a satellite torus that performs twelve complete turns around the ξ axis before closing. Tori that have 9, 10, 11 and 13 turns before closing have also been easily detected. Similar structures also would appear in the left panel under a sufficiently high magnification. Finally for the right panel, where $a = 3.7$, the regular region has eroded, though there are still some tori around the central invariant curve. Moreover, there appears what seems to be a period-five elliptic invariant circle surrounded by tori that are satellites of the central structure.

3. A volume-preserving map with accelerator modes

In this section we construct a 3D angle-action map with accelerator modes. Our goal is to study the stickiness of a bubble of regular orbits in an otherwise seemingly fully chaotic phase space. Hence, we look for a family f_ε of VPM of $\mathbb{T}^2 \times \mathbb{R}$, that smoothly projects to a map $\tilde{f}_\varepsilon$ on $\mathbb{T}^3$ under Π, recall (2).

To construct our model, we choose f_ε so that it fulfills the following three requirements (already sketched in section 1):

R1 The map has an integrable limit $\varepsilon \to 0$, where the phase space is foliated by horizontal rotational invariant tori (RIT) $\{z = \text{const}\}$ and the restriction of the dynamics on each RIT is topologically conjugate to a rigid rotation. Near this limit, some of these tori should persist: a volume-preserving KAM theorem should apply [12, 58].

R2 For $\varepsilon = n \in \mathbb{N}_+$, the origin $P_+ = (0,0,0)$ is a fixed point of $\tilde{f}_n$, and for all $m \in \mathbb{Z}$, $f_n^q(0,0,m) = (0,0,m+nq)$. Hence, the origin is an FPAM, recall definition 1.

R3 Near the creation of the FPAM, the parameter $\kappa_n = \varepsilon - n$ unfolds a Hopf-one bifurcation. Hence, for $0 < \kappa_n \ll 1$, a small volume of regular orbits may exist near P_+. We will define the family f_ε in such a way that its Taylor expansion around P_+ for $\varepsilon = n + \kappa_n$, $n \in \mathbb{N}_+$ is locally conjugate to a map in the family $M_{\varphi,a}$ (9), where the higher order terms (in u, v, w) depend on n in such a way that they tend to vanish as $n \to \infty$, see proposition 1 in section 3.2.

3.1. Shearing functions

In this subsection we construct a concrete family of maps satisfying the requirements **R1**– **R3** using the composition of three shears (8).

The second and third requirements are achieved for the family

$$f_\varepsilon : \begin{pmatrix} x \\ y \\ z \end{pmatrix} \mapsto \begin{pmatrix} x' \\ y' \\ z' \end{pmatrix} = \begin{pmatrix} x + \mu \sin(2\pi y) + \psi(z') \\ y + \nu \sin(2\pi z') \\ z + \varepsilon\left(\cos(2\pi x) - \beta \sin(2\pi y)\right) \end{pmatrix}, \tag{13}$$

where μ, ν, β are parameters. We assume that ψ is a degree-one circle map (i.e. $\psi(z+1) = z + \psi(z)$) that satisfies

$$\psi(0) = \psi'(0) = 0. \tag{14}$$

To satisfy **R1** the function $\psi(z)$ could simply be z itself, and—as we will show below— **R2** is automatically fulfilled when $\psi(0) = 0$. The condition **R3** requires, however, that the first derivative vanishes at the location of the FPAM, see section 3.2.

From the expression (13) it is clear that $P_+ = (0,0,0)$ and $P_- = (\frac{1}{2}, 0, 0)$ are fixed points of the projection $\tilde{f}_n$. Under f_n, P_+ goes up by n units and P_- goes down by n units in z upon each iterate (see also remark 2). After the Hopf-one bifurcation the point P_+ gives rise to a pair of FPAM, to be denoted by $P_+^{l,r}$ in section 3.2. It would be nice to have similar properties for P_-, i.e, for it to give rise to a FPAM pair $P_-^{l,r}$ as well. A simple way to obtain this is by choosing ψ to be an odd function: $\psi(-z) = -\psi(z)$. This is not necessary to unfold the bifurcation, but it is simpler to have similar bubbles created near P_+ and P_-, one going up and the other down.

To satisfy (14) and to have the odd character of ψ we choose $\psi(z)$ to be an odd, degree-one map given by

$$\psi(z) = z + \sum_{j=1}^{7} a_j \sin(2\pi j z). \tag{15}$$

The choice of the function ψ above is justified in appendix A, where appropriate values for the Fourier amplitudes, a_j, are also given, see (A.1).

To ensure that (13) fulfills **R1** we can take

$$\mu = \varepsilon\tilde{\mu}, \quad \tilde{\mu} = \mathcal{O}(1).$$

The point is that when $\varepsilon = \mu = 0$ each horizontal two-torus $\{z = \text{const}\}$ is invariant, and the dynamics on each torus is a rigid rotation with rotation vector $\omega = (\psi(z), \nu\sin(2\pi z))$.

The first requirement is then satisfied if f_ε satisfies the hypotheses of the volume-preserving KAM theorem [12, 58]. This theorem is stated for an analytic map of the form (4). Our model (13) can be written in this form upon taking

$$\begin{aligned} \Omega(z) &= (\psi(z), \nu\sin(2\pi z)), \\ \varepsilon h_1(x,y,z) &= \Omega_1(z') - \Omega_1(z) + \varepsilon\tilde{\mu}\sin(2\pi y), \\ \varepsilon h_2(x,y,z) &= \Omega_2(z') - \Omega_2(z), \quad \text{and} \\ h_3(x,y,z) &= \cos(2\pi x) - \beta\sin(2\pi y). \end{aligned}$$

In addition, we have to check if the following two necessary conditions hold for f_ε [58]:

1. *Intersection property*. The image under f_ε of any homotopically non-trivial two-torus, sufficiently close to a horizontal torus $\{z = \text{const}\}$, intersects itself. This is achieved because $h_3(x, y, z)$ has zero average with respect to the angles (x, y).
2. *Nondegeneracy condition*. There exists a $k \in \mathbb{N}$, such that the frequency map satisfies a twist-like, nondegeneracy condition:

$$\operatorname{rank}\begin{pmatrix} \Omega_1'(z) & \Omega_2'(z) \\ \vdots & \vdots \\ \Omega_1^{(k)}(z) & \Omega_2^{(k)}(z) \end{pmatrix} = 2. \tag{16}$$

If $|\varepsilon| \ll 1$, $\mu = \mathcal{O}(\varepsilon)$, and $\psi(z)$ is chosen to satisfy (16), KAM theory implies that f_ε will have a Cantor set of RIT that are deformations of the horizontal tori that exist for $\varepsilon = 0$.

Remark 1. By contrast with the case of symplectic maps, since the number of actions is less than the number of angles ($l < d$), the frequency map $\Omega : \mathbb{R}^l \to \mathbb{T}^d$ cannot be surjective. Hence one cannot assure the persistence of a RIT with prescribed frequencies. Thus KAM

theory does not guarantee the persistence of a torus with a given rotation vector, only that there are many tori when $\varepsilon \ll 1$.

Remark 2. For the map (4), the condition that h_3 has zero average means that there is zero net volume flux through any rotational torus, which implies the intersection property. For the map (13), this condition also implies that for each FPAM with positive acceleration, e.g. P_+, there is another with negative acceleration. In our case, the corresponding downwards FPAM is located at $P_- = (\frac{1}{2}, 0, 0)$.

The nondegeneracy condition (16) may have a different minimal value of k in different ranges of z. For example, for f_ε, (16) does not apply for $k = 2$ at $z = 0$ since $\psi'(0) = \psi''(0) = 0$. However, it will hold for $k = 3$ so long as $\psi^{(3)}(0) \neq 0$. This may happen for other values of z depending on the choice of $\psi(z)$. Indeed, since $\psi(z)$ is odd, (16) for $k = 2$ is also violated at $z = \frac{1}{2}$. Consequently, we expect that there will be more prominent chaotic zones near $\{z = 0\}$ and $\{z = \frac{1}{2}\}$ for small $\varepsilon > 0$. For the choice (15) with the coefficients (A.1), the condition (16) is violated for $k = 2$ at ten additional points $z \in (0, 1)$, but one can check that it does hold for $k = 3$ at all of these points.

To verify that (13) satisfies **R2**, we can compute its fixed points and accelerator modes. For any values of the parameters, there are four fixed points located at $(\frac{1}{4}, 0, 0)$, $(\frac{1}{4}, \frac{1}{2}, 0)$, $(\frac{3}{4}, 0, 0)$, and $(\frac{3}{4}, \frac{1}{2}, 0)$. Since the map preserves volume, all of these are generically unstable: the product of the three multipliers of Df_ε is one, $\lambda_1\lambda_2\lambda_3 = 1$. So, unless all three have modulus one, there will be at least one unstable multiplier. Additional fixed points correspond to accelerator modes. The following lemma is proved in appendix B.

Lemma 1. *Suppose that*

$$0 < |\mu| < \frac{1}{2}, \qquad 0 < |\nu| < \frac{1}{2}. \tag{17}$$

Then for each $\varepsilon = n \in \mathbb{N}_+$ f_ε has a Hopf-one bifurcation that creates four FPAM. Two of these, $P_+ = (0,0,0)$ and $Q_+ = (0, \frac{1}{2}, 0)$, accelerate upwards, and two, $P_- = (\frac{1}{2}, 0, 0)$ and $Q_- = (\frac{1}{2}, \frac{1}{2}, 0)$, accelerate downwards.

Finally, we note that the map f_ε commutes with the involution R: $f_\varepsilon \circ R = R \circ f_\varepsilon$, where R is given by

$$R(x, y, z) = (\frac{1}{2} - x, -y, -z). \tag{18}$$

Indeed, this follows for any map of the form (8) when the shears are odd about the point $(\frac{1}{4}, 0, 0)$, which is a fixed point of R. In particular $R(P_+^l) = P_-^r$ and $R(P_+^r) = P_-^l$. Also the manifolds associated to the $P_-^{r,l}$ are obtained under the symmetry R from the manifolds of $P_+^{l,r}$. See section 5.1 for details.

For the remainder of the paper, we will not vary μ with ε, but will return to the form (13) for a fixed small value of μ. We think of ε as the primary parameter, and take (μ, ν, β) as 'fixed'.

3.2. Local dynamics near an accelerator mode

In this section we study the local dynamics around the FPAM of f_ε (13) when ε is near $n \in \mathbb{N}_+$. This is done by expanding about the FPAM to quadratic order and rescaling the variables.

To motivate the scaling, consider for example, the dynamics around $P_+ = (0, 0, 0)$. Let $\varepsilon = n + \kappa_n$, where $\kappa_n > 0$ is small. Then P_+ bifurcates into a pair of new FPAM located at $P_+^{l,r} = (x^{l,r}, 0, 0)$ where (13) implies that $x^{l,r}$ must satisfy $(n + \kappa_n)\cos(2\pi x^{l,r}) = n$. When κ_n is small, this implies

$$x^{l,r} = \mp\frac{1}{\pi}\sqrt{\frac{\kappa_n}{2n}} + \mathcal{O}(\kappa_n). \tag{19}$$

This scaling motivates the introduction of a new parameter $\delta = n\kappa_n$ and of the scaled phase variables $n(x, y, z)$, so that the distance between the new FPAM becomes $\mathcal{O}(\sqrt{\delta})$.

Proposition 1. *Given μ, ν, β, let $\varepsilon = n + \delta/n$ and P be any of the accelerator modes of lemma 1. Thus δ/n measures the distance from the birth of P. Define new phase variables $(\xi, \eta, \zeta) = n\,((x, y, z) - P)$, and let $f_\delta^*(\xi, \eta, \zeta)$ be the projected map $\tilde{f}_{n+\delta/n}$ in the new variables. Then the following holds.*

1. *The Taylor expansion of f_δ^* around the origin can be written as $f_\delta^* = L + \mathcal{O}(n^{-1})$, where L is a quadratic volume-preserving map.*
2. *An additional normalization $(u, v, w) = (\alpha_\xi\xi, \alpha_\eta\eta, \alpha_\zeta\zeta)$ conjugates L to the Michelson map (9) for suitable parameters φ and a.*

Proof. For the moment, let us restrict ourselves to the dynamics around P_+. In the variables $(\xi, \eta, \zeta) = n(x, y, z)$, map f_δ^* becomes

$$\begin{pmatrix}\xi'\\ \eta'\\ \zeta'\end{pmatrix} = \begin{pmatrix} \xi + n\mu\sin\left(2\pi\frac{\eta}{n}\right) + n\psi\left(\frac{\zeta'}{n}\right) \\ \eta + n\nu\sin\left(2\pi\frac{\zeta'}{n}\right) \\ \zeta + n\left(\left(n + \frac{\delta}{n}\right)\left(\cos\left(2\pi\frac{\xi}{n}\right) - \beta\sin\left(2\pi\frac{\eta}{n}\right)\right) - n\right)\end{pmatrix}, \tag{20}$$

where $-n$ in the third component is due to the projection to the torus. Expanding around $(0, 0, 0)$ gives

$$f_\delta^* = L_{\delta,\beta} + \mathcal{O}(n^{-1}),$$

where

$$L_{\delta,\beta} : \begin{pmatrix}\xi'\\ \eta'\\ \zeta'\end{pmatrix} = \begin{pmatrix} \xi & + & 2\pi\mu\eta \\ \eta & + & 2\pi\nu\zeta' \\ \zeta & + & \delta - 2\pi^2\xi^2 - 2\pi\beta n\eta\end{pmatrix}. \tag{21}$$

Note that n has disappeared, except for the last term, proportional to βn.

The same procedure can be applied to the remaining three FPAM, but one has to take into account some changes of sign due to expanding the trigonometric functions around π instead of 0, and the fact that P_- and Q_- jump downwards. Table 1 summarizes the scalings and gives the form of L one obtains after this procedure. Note that the only difference in the final form is that $\beta \to -\beta$ for the $Q_\pm$ FPAM.

Applying the additional normalization $(u, v, w) = (\alpha_\xi\xi, \alpha_\eta\eta, \alpha_\zeta\zeta)$ to (21) shows that $L_{\delta,\beta} \simeq M_{\varphi,a}$, the Michelson map (9), if we choose

Table 1. Scalings to obtain the quadratic map L near an FPAM.

FPAM	(ξ,η,ζ)	Map
$P_+ = (0,0,0)$	$n(x,y,z)$	$L_{\delta,\beta}$
$P_- = (\frac{1}{2},0,0)$	$n(\frac{1}{2}-x,-y,-z)$	$L_{\delta,\beta}$
$Q_+ = (0,\frac{1}{2},0)$	$n(-x,y-\frac{1}{2},z)$	$L_{\delta,-\beta}$
$Q_- = (\frac{1}{2},\frac{1}{2},0)$	$n(x-\frac{1}{2},\frac{1}{2}-y,-z)$	$L_{\delta,-\beta}$

$$\alpha_\xi = \pi\left(\tfrac{2}{\delta}\right)^{\frac{1}{2}}, \qquad \alpha_\eta = \pi\left(\tfrac{4\mu^2}{\delta^2\nu}\right)^{\frac{1}{3}}, \qquad \alpha_\zeta = \pi\left(\tfrac{32\mu^2\nu^2}{\delta^5}\right)^{\frac{1}{6}}, \tag{22}$$

$$\varphi = \pi\left(32\mu^2\nu^2\delta\right)^{\frac{1}{6}}, \qquad a = \beta n\left(\tfrac{2\nu}{\delta\mu^2}\right)^{\frac{1}{3}}. \tag{23}$$

These expressions are the same for the other fixed points except that for $Q_\pm$, the parameter a changes sign since, by table 1, $\beta \to -\beta$. □

Remark 3. There are some important aspects of the local form that are worth noting:

- The fixed points of (21), at $(\pm\sqrt{\frac{\delta}{2\pi^2}},0,0)$, collide as $\delta \to 0$.
- For fixed β, the parameter a as given in (23) grows linearly with n. Recall, from section 2.4, that a bubble of stability for $M_{\varphi,a}$ appears when $a\varphi^2 = 4\pi^2\beta n\nu \in (0,4)$. Hence, for the one-parameter family f_ε, we can only expect to detect a finite number of such stability regions, those born at $\varepsilon = n < (\beta\pi^2\nu)^{-1}$.
- A bubble of stability occurs near $P_\pm$ when $\beta\nu > 0$, but since the sign of a in (23) changes for $Q_\pm$, the bubble will occur near $Q_\pm$ when $\beta\nu < 0$. Hence the requirement **R3** is satisfied.

Proposition 1 implies that $M_{\varphi,a}$ encodes the local dynamics near an FPAM under the proper scaling. To do this, we think of f_ε^* as a two-parameter family $f^*_{\varepsilon,\beta}$. A final scaling of the parameter β implies the following.

Corollary 1. *For given μ,ν let $\beta_n = \tilde\beta/n$ and $\varepsilon_n = n + \delta/n$ for fixed $\tilde\beta$ and δ. Then there is a ball around $P_\pm$ ($Q_\pm$) inside of which the Taylor expansion of $f^*_{\varepsilon_n,\beta_n}$ converges, as $n \to \infty$, to a map that is conjugate to $M_{\varphi,a}$ ($M_{\varphi,-a}$), where $\varphi = \pi(32\mu^2\nu^2\delta)^{1/6}$ and $a = \tilde\beta\left(2\nu/\delta\mu^2\right)^{1/3}$.*

4. Diffusion in the presence of a bubble: a case study

In this section we study the diffusive properties of chaotic orbits of (13) when there is a bubble of stable orbits near some of the FPAM, see appendix B. To this end, we perform numerical simulations for $0 < \varepsilon - 1 \ll 1$.

4.1. Choosing parameters

We use the function $\psi(z)$ introduced in appendix A and choose values of the parameters μ,ν and β of f_ε in (13) so that

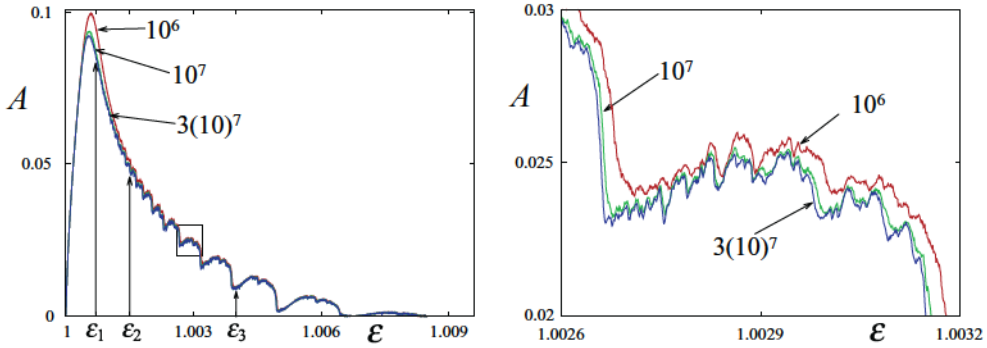

Figure 2. The fraction of bounded orbits around the accelerator mode P_+ of f_ε as a function of ε for parameters (24). Initial conditions are chosen with $z = 0$ in the box $(x, y) \in [-0.024, 0.024] \times [-0.12, 0]$. The three curves correspond to different maximal number of iterates $T_{\max}$, as labelled. Left: the bounded fraction for $\varepsilon = 1 + \kappa_1$, for $\kappa_1 \in [10^{-6}, 0.0096]$ in steps of 10^{-6}. The labelled values $\varepsilon_1 = 1.0007$, $\varepsilon_2 = 1.0015$ and $\varepsilon_3 = 1.004$ are studied in section 4.4. Right: magnification near $\varepsilon = 1.003$ of the box in the left figure.

1. For $\varepsilon - 1 > 0$ and small the local map $M_{\varphi,a}$ (9) around $P_\pm$, satisfies $a\varphi^2 = 4\beta\pi^2\nu \in (0, 4)$.
2. The critical parameter value, $\varepsilon_{\text{crit}}$, at which the last RIT of f_ε is destroyed is as large as possible.

The first requirement is a necessary condition to ensure that there is a region of regular motion near the FPAM $P_\pm$. The second requirement, ensures that the map is not too chaotic. Note that the value $\varepsilon_{\text{crit}}$ is analogous to Greene's critical value for Chirikov's standard map (3) [26]. Such values have been found for VPM in [23, 39].

After an exploration of the dynamics for various parameters, we choose

$$\mu = 0.01, \qquad \nu = 0.24, \quad \text{and} \quad \beta = 0.12. \tag{24}$$

For this choice, $a\varphi^2 \approx 1.137n$, so we only expect to detect a region of regular motion around $P_\pm$ for $n < 4$, recall remark 3.

For the parameters (24), we conjecture that[4] $\varepsilon_{\text{crit}} \in (0.093, 0.094)$. To determine this, we iterated a set of initial conditions in $\mathbb{T}^2 \times [0, 1]$ for $T = 2 \cdot 10^7$. Each initial condition was classified first as either escaping or non-escaping from $z \in [0, 1]$. Those that did not escape were classified as either chaotic or regular using an approximation of the Lyapunov exponent. If this approximation was small, so that the orbit appeared to be regular, we checked whether it could be on a RIT by looking to see if its (x, y) projection completely filled all the pixels on a 400×400 grid.

4.2. Regular region around the accelerator mode

We focus on the effect of the FPAM that appear for $\varepsilon = 1$, since they are expected to have the largest bubble. Figure 2 shows the relative measure of bounded orbits near P_+ that start in the half-plane $z = 0$, $y \leqslant 0$. We considered a 400×360 grid in $(x, y) \in [-0.024, 0.024] \times [-0.12, 0]$. This range is chosen accordingly to the position of the fixed points of $\tilde{f}_\varepsilon$ that bifurcate from the origin at $\varepsilon = 1$. We iterate the centers of the grid cells up to a time $T_{\max}$, and declare that the

[4] This critical value is not too far from Greene's critical value $k_{\text{crit}} \approx 0.971\,635/(2\pi) \approx 0.154\,641$.

orbit escapes from the bubble if at any time $\max(|x|, |y|, |z|) > 0.25$. The left panel of the plot shows values of ε over the full range where a stable accelerator mode with $n = 1$ is detected. The fraction of bounded orbits exhibits a number of sudden decreases, and an enlargement of some of these are shown in the right panel of the figure. These drops in bounded area correspond to the breakdown of an outermost invariant two-torus that allows previously confined motion to escape from the bubble.

4.3. Diffusion in the chaotic zone: expectations

After the breakdown of the last RIT near $\varepsilon_{\text{crit}} \approx 0.094$, the phase space seems to become much more chaotic. In particular, for $0.2 < \varepsilon < 1$ we have numerically checked that any regular component in the phase space is below pixel size ($1/400^2$ squared units in $\mathbb{T}^2$). For ε in a subinterval of $[1, 1.009]$ one detects the presence of a bubble of stability around $P_\pm$, recall figure 2. In this section we investigate the diffusion in the z variable for $\varepsilon \in [0.2, 1.8]$.

Outside the range in ε where the accelerator-mode bubble appears, we expect an exponential decay of correlations giving 'normal' diffusion in the action variable z, namely, that the standard deviation after T iterates

$$\sigma_T = \left(\left\langle (z_T - z_0)^2 \right\rangle - \langle z_T - z_0 \rangle^2 \right)^{\frac{1}{2}} \sim T^\chi, \tag{25}$$

where $\chi = \frac{1}{2}$, so that the limit

$$D = \lim_{T\to\infty} \frac{\sigma_T^2}{2T}, \tag{26}$$

exists. Here $\langle \cdot \rangle$ stands for the average over an ensemble of initial conditions (x_0, y_0, z_0), which we usually take to be uniform on some domain of $\mathbb{T}^3$ outside bubbles of stability, and $(x_T, y_T, z_T) = f_\varepsilon^T(x_0, y_0, z_0)$. The one-step coefficient, known as the *quasilinear approximation*, can be easily evaluated as

$$D_{ql} = \frac{1}{2} \left\langle (z' - z)^2 \right\rangle = \int_{\mathbb{T}^2} (z' - z)^2 = \frac{\varepsilon^2}{4}(1 + \beta^2), \tag{27}$$

using (13).

The behavior of the action diffusion when there is a bubble, e.g. for $\varepsilon \in [1, 1.009]$, can be expected to be very different. Indeed as was discussed in section 2.1, the hierarchical island-around-island structure of the 2D case gives rise to a power-law behavior of the trapping time distribution [42], which, in turn, gives rise to anomalous diffusion [1]. However for the 3D case, the way that tori in a bubble are organized by their rotation vectors is not known, so we do not have the ability to create a model similar to the 2D one.

4.4. Numerical experiments

In this section we describe the results of the numerical experiments for diffusion and trapping statistics. In section 4.4.1 we will show that the presence of accelerator-mode orbits gives rise to anomalous diffusion of the action. In section 4.4.2 we show that the trapping statistics appears to have power-law decay $\mathcal{P}_\varepsilon(t) \sim t^{-b}$, $b > 2$. Both of these results are consistent with the 2D case [37, 38].

In order to avoid choosing initial conditions inside a bubble, we take them on a fundamental domain of the right branch of the 1D unstable manifold of the fixed point $(\frac{3}{4}, 0, 0)$. When

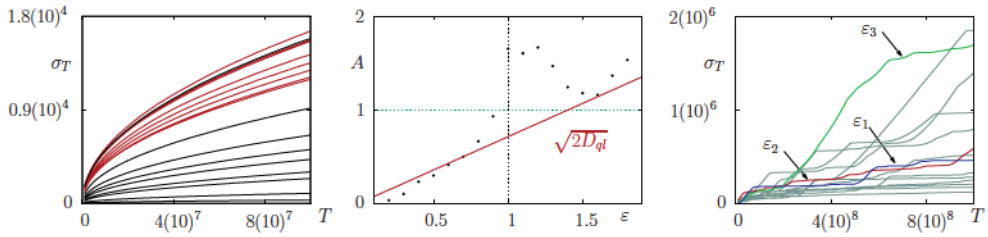

Figure 3. The standard deviation σ_T as ε varies. Left: the standard deviation as a function of T for nine values, $\varepsilon = 0.2(0.1)1$, in black, and eight values, $\varepsilon = 1.1(0.1)1.8$, in red. Center: Growth rate A, defined by $\sigma_T \sim A\sqrt{T}$ for these ε values. Right: the standard deviation for fourteen (non-equispaced) $\varepsilon \in [1.0005, 1.0055]$. The labelled curves correspond to $\varepsilon_1 = 1.0007$ (blue), $\varepsilon_2 = 1.0015$ (green) and $\varepsilon_3 = 1.0040$ (red).

$\varepsilon = \mathcal{O}(1)$ and μ, ν and β as given in (24), this point is a saddle with a 1D unstable manifold and a 2D stable manifold. We choose $N = 10^6$ to 10^7 initial conditions on $W^u(\frac{3}{4}, 0, 0)$, logarithmically equispaced over a distance interval $[10^{-9}, 10^{-8}]$ from the fixed point.

Each initial condition was iterated between 10^8 and 10^{11} times, depending on the observed behavior, and we compute the following two observables:

1. *The standard deviation*. Anomalous diffusion of the action is detected by examining the growth rate of σ_T, (25). In a phase space that is seemingly fully chaotic and has no accelerator modes, one expects the limit (26) to exist and that D should be near the quasilinear value (27). When there are accelerator modes one expects a faster growth so that the limit (26) does not exist.
2. *The trapping statistics*. We kept track of the number of consecutive iterates that an orbit remains close to a bubble, i.e. in the union $\mathcal{W} = \mathcal{W}_+ \cup \mathcal{W}_-$ of neighborhoods of P_+ and P_-. For most of cases, the neighborhoods

$$\begin{aligned} \mathcal{W}_+ &= \{(x,y,z) \ : \ |x| \leqslant 0.024, |y| \leqslant 0.12, |z| \leqslant 0.08\}, \\ \mathcal{W}_- &= \{(x,y,z) \ : \ |x - \frac{1}{2}| \leqslant 0.024, |y| \leqslant 0.12, |z| \leqslant 0.08\}, \end{aligned} \tag{28}$$

appear to completely contain the bubbles; however, we modify these regions slightly in section 5.2. Note that the set $\mathcal{W}_+ \cap \{z = 0, y \leqslant 0\}$ was used in figure 2. The probability of having a stay of exactly length t near the bubbles is

$$\mathcal{P}_\varepsilon(t) = \text{Prob}\left((x_j, y_j, z_j \bmod 1) \begin{cases} \in \mathcal{W}, & j \in [i, \ldots, i+t], \\ \notin \mathcal{W}, & j \in \{i-1, i+t+1\} \end{cases} : i \in [1, T-t] \right). \tag{29}$$

This is the analogue of the trapping statistic (6) used in the area-preserving case.

We computed $\mathcal{P}_\varepsilon(t)$ for an orbit of length $T = 2^{26.6} \approx 10^8$ by partitioning this interval into subintervals that are logarithmically equispaced, i.e. $I_i = [2^{0.1i}, 2^{0.1(i+1)})$ for i up to 265. We declare an orbit to be 'trapped' around a bubble if it remains in $\mathcal{W}$ for at least $t_0 = 128$ consecutive iterates, so we start with $i = 70$, corresponding to this shortest trapping segment.

A histogram is constructed for the number of trapped orbit segments in $\mathcal{W}$ of length $t \in I_i$. Normalizing this gives the probability, $\mathcal{P}_\varepsilon$ for $t = 2^{0.1(i+1/2)}$, in the logarithmic middle of I_i.

4.4.1. Normal and anomalous diffusion. The left panel of figure 3 shows the standard deviation (25) as a function of T for seventeen values of $\varepsilon \in [0.2, 1.8]$. When $\varepsilon < 1$ (black curves)

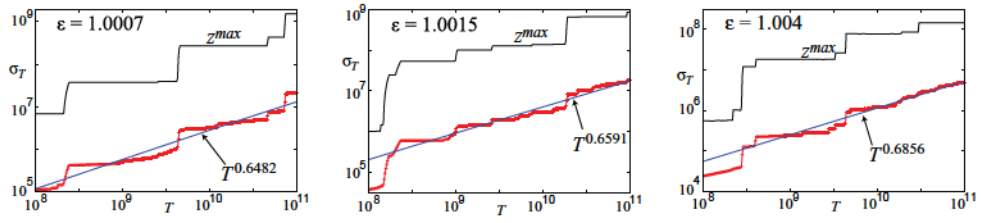

Figure 4. The standard deviation as a function of T (red curves) on a log-log scale for the ε values shown. A least squares linear fit (blue) gives the slopes, χ, indicated in each plot. The upper curves (black) show the maximal value of $|z_T|$ among the $N = 10^4$ initial conditions iterated.

Table 2. Exponent χ for the standard deviation (25), and b for the exit time distribution (6)–(29) obtained from the numerical experiments on the map f_ε (13) for the values ε_1, ε_2, and ε_3. See section 5.3 concerning the last column.

ε	χ	b	$\chi + b/2$
1.0007	0.6482	2.0989	1.6977
1.0015	0.6591	2.4243	1.8713
1.004	0.6856	2.5630	1.9671

there are no accelerator modes and when $\varepsilon = 1$, there are no bubbles. When $\varepsilon \geqslant 1.1$ (red curves) the accelerator bubbles have already disappeared.

From this data it seems reasonable to assert that $\sigma_T \sim \sqrt{T}$. To check this claim, we performed least squares fits of the full data sets for each displayed ε to a function of the form $\sigma_T = AT^\chi$. For all fits, we found $\chi \in (0.4975, 0.5025)$, close to the expected value of $\frac{1}{2}$. The corresponding values of A are displayed in the central plot of figure 3 (black dots), together with the estimate $\sqrt{2D_{ql}}$ (in red), recall (27). The deviation between the numerically obtained values and the quasilinear prediction is larger for $\varepsilon \approx 1$ and the effect of the accelerator mode can be seen even when there is no bubble. Note that when $\varepsilon < 1$ the diffusion coefficient appears to grow nearly linearly with ε, but at a slope larger than the quasilinear estimate. Recall that for Chirikov's standard map, the quasilinear prediction is a better approximation for large parameter values [13, 46, 49, 54], but we have not checked values of ε larger than 1.8 here.

In the right panel of figure 3 we see that when $\varepsilon \in [1.0005, 1.0055]$—when the FPAM around $P_\pm$ have stable bubbles—σ_T grows more rapidly than $\sqrt{T}$ and depends irregularly on ε. Intervals of linear growth, corresponding to very long trapping segments, are interspersed with intervals of slower growth where the orbit is not trapped or has only short trapped intervals. The considerable variability in the growth of σ_T as a function of ε is presumably due to the strong dependence of the geometry of the bubbles on ε and to the sensitivity of the long trapping times to chaos.

To assess the anomalous diffusive properties of f_ε we iterated $N = 10^4$ initial conditions to $T = 10^{11}$ to compute σ_T for the three particular values, ε_1, ε_2 and ε_3—the highlighted values in figure 3. Logarithmic plots of the averaged σ_T are shown in figure 4. In these plots, a trapping interval can cause jumps in

$$z_T^{\max} = \max_{(x_0,y_0,z_0)} (|z_T|),$$

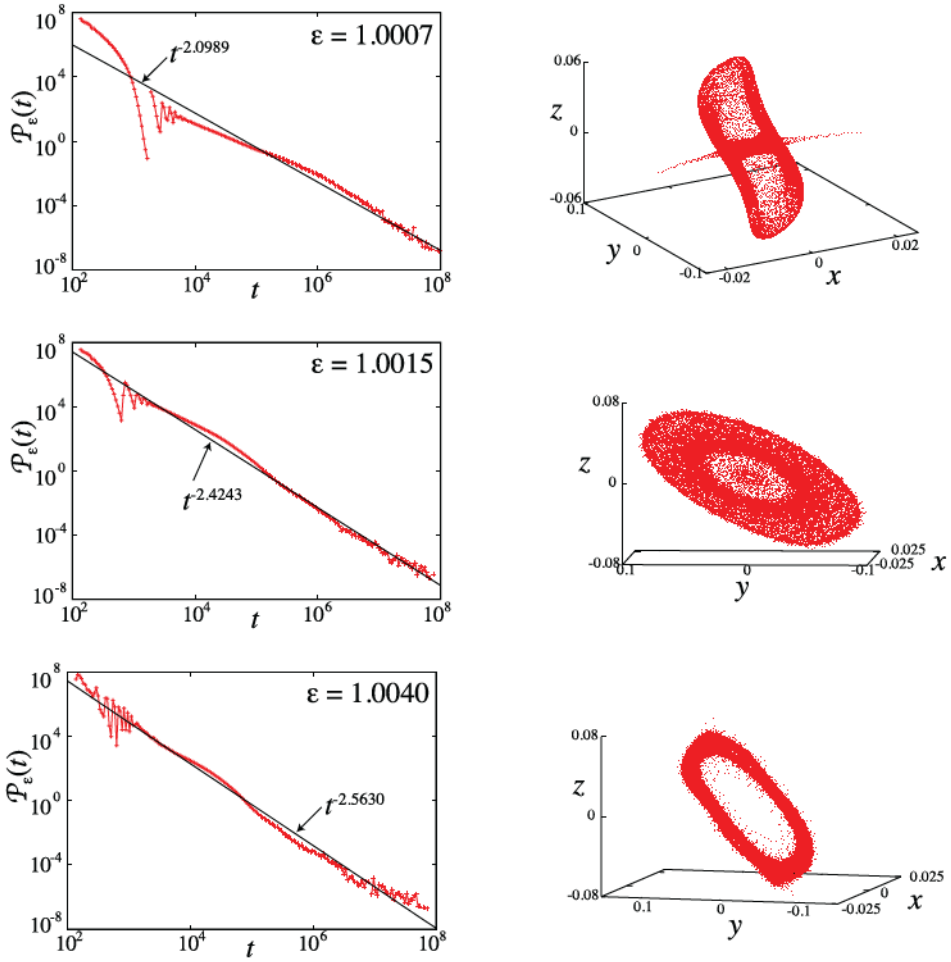

Figure 5. Trapping statistics versus time for $\varepsilon = 1.0007, 1.0015$ and 1.0040. Each right panel shows an example of a trapped orbit near the bubble of P_+ for the corresponding ε value on the left.

sometimes up to an order of magnitude over a time interval of order 10^8. In the previous definition (x_0, y_0, z_0) ranges in the set of initial conditions.

For the three ε values of figure 4, a fit to $\sigma_T = AT^\chi$ over $10^8 < t < 10^{11}$ gives exponents shown in table 2. All are significantly larger than the diffusive value $\frac{1}{2}$. Note that the value of χ depends on the range of values used for T. In particular, it abruptly changes if we end the simulation just before or after a big jump.

4.4.2. Trapping statistics. The trapping statistics (29) for bubbles at $\varepsilon_1, \varepsilon_2$, and ε_3 are shown in log-log plots in figure 5. In all cases it seems plausible to assume, following (6), that $\mathcal{P}_\varepsilon(t) \sim t^{-b}$, with some fluctuations. A least-squares fit (performed over the entire range) to a straight line (black) gives the exponents shown in table 2. Repeating the computations for ε_1 with $N = 10^6$ initial conditions and 10^{10} iterates gives the same value of b to three decimal figures. Such a power law decay was previously observed for orbits started near a 2D torus in

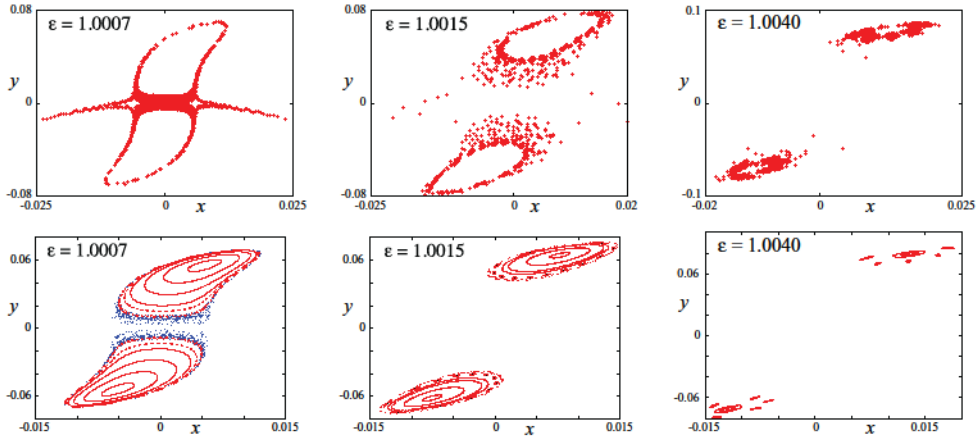

Figure 6. Slices through orbits near the bubbles of figure 5. Points on the orbits with $|z| < r$ are shown projected onto the (x, y) plane. Top row: temporarily trapped orbits for $r = 0.01$ (left and middle) and $r = 0.02$ (right). Bottom row: trapped orbits inside the bubbles (red, $r = 10^{-4}$) and, for $\varepsilon = 1.0007$, an escaping orbit (blue, $r = 10^{-4}$). For the middle plot the value of $r = 10^{-7}$ has been used for the black points.

a volume-preserving map in [48]; by contrast in [53] the authors observe an exponential decay of trapping statistics in a different VMP.

Each panel in the right column of figure 5 shows a typical orbit trapped near P_+ for the same ε as the left column. Slices near $z = 0$ of these same orbits are shown in the (x, y) plane in the top row of figure 6. The bottom row of this figure shows slices through some regular orbits in the P_+ bubble. Recall that when $\kappa_1 > 0$ the point P_+ bifurcates into a pair of accelerating orbits $P_+^{l,r} = (x^{l,r}, 0, 0)$ (19).

In section 2.4 we noted that P_+^r (P_+^l) has a 1D stable (unstable) invariant manifold and a 2D unstable (stable) manifold. These seem to play an important role in the trapping, and we will discuss this in section 5.1.

For our three standard values of the parameter, we observe the following.

- $\varepsilon_1 = 1.0007$. Close to the birth of the bubble (recall figure 2) the invariant manifolds of $P_+^{l,r}$ can be clearly guessed in figure 6. The longest trapped orbits approach the bubble along $W^s(P_+^r)$, then follows a trajectory that seems to cover a 2D torus, finally escaping along $W^u(P_+^l)$.
- $\varepsilon_2 = 1.0015$. Further away from the birth of the bubble there are prominent satellite tori outside the main tori, and the longest trapped orbits appear to be primarily stuck around such satellites: in figure 6 this region has the highest density. Each of these satellites encloses an elliptic invariant circle giving what seems to be a period-twelve orbit in the section (the black points in the bottom middle panel of figure 6). In fact, there are six invariant curves of f_ε^6, one the image of the other under f_ε. Under f_ε^6 each of these curves closes after two revolutions around the x axis. The central region of the bubble, near the 1D manifolds of $P_+^{l,r}$, has a lower density, but it still seems to play a role in its stickiness.
- $\varepsilon_3 = 1.0040$. Now the regular region around the bubble is almost destroyed, but one still expects trapping around the main tori or satellite tori. The orbit shown in figure 6 seems to be trapped around a family of tori that surrounds a single elliptic invariant curve, which closes after five revolutions around the x axis.

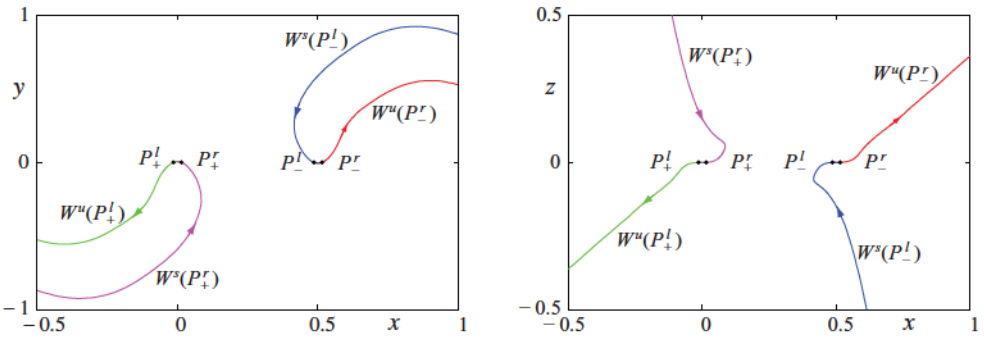

Figure 7. One-dimensional manifolds of $P_\pm^{r,l}$ for $\varepsilon_3 = 1.004$ projected into the (x, y) (left) and (x, z) (right) planes, shown for $x \in [-0.5, 1]$.

Recall that by proposition 1, the Michelson map (9) is a quadratic approximation near $P_\pm$ for the family (13). Though this approximation is less accurate when $n = 1$, there is a coordinate change of the form $(x, y) \mapsto (x - G(\varepsilon)y^3, y)$, for suitable $G(\varepsilon)$, that brings the plots in figure 6 closer to those in figure 1 for the Michelson map.

5. Discussion

In this section we discuss in more detail how chaotic orbits approach the vicinity of a bubble. We also discuss how the results of the previous section fit with, and deviate from, existing theoretical approaches, suggesting a possible approach to deal with the discrepancies.

5.1. Entering and exiting the bubbles

As we noted above, the entrance and exit routes for a bubble often correspond to the 1D manifolds of the fixed points $P_\pm^{r,l}$ of $\tilde{f}_\varepsilon$. Numerical computations of these manifolds are shown in figure 7 for ε_3. Qualitatively similar curves are obtained for other parameters. Recall that the reversing symmetry (18) implies that the invariant manifolds of $P_-^{r,l}$ can be obtained from those of $P_+^{r,l}$ using the reversor (18), and this symmetry is clearly manifest in the figure. When a bubble is present, points on outer branches of the unstable 1D manifolds do not appear to return to a neighborhood of the bubbles in a small number of iterations. The implication is that these manifolds correspond to entrance and exit routes for the neighborhood of a bubble.

A large fraction of orbits that get trapped in $\mathcal{W}_+$ (28) approach P_+^r along the right branch of $W^s(P_+^r)$, the purple curve in figure 7. They then move away from this point along its 2D unstable manifold, $W^u(P_+^r)$ (not shown in the figure). This manifold curves towards the neighboring saddle-focus, P_+^l. The 2D stable manifold of this point similarly curves towards P_+^r, and so these two manifolds intersect. Some orbits are thus funneled along $W^s(P_+^l)$ towards P_+^l. They finally escape the bubble close to the left branch of $W^u(P_+^l)$, the green curve in the figure. Though the incoming orbits to $\mathcal{W}_+$ need not be very close to $W^s(P_+^r)$, the attraction of $W^s(P_+^l)$ tends to make escaping orbits closely follow $W^u(P_-^r)$. Moreover, the length of the trapped segment is longer if an orbit is closer to the stable manifolds, since such orbits spend more time near the saddle-foci. By symmetry the same explanation applies to incoming

and escaping orbits for the region $\mathcal{W}_-$ around $P_-^{l,r}$. The case $\varepsilon = 1.0007$ in figure 5 and its corresponding slice around $z = 0$ in figure 6 illustrate this situation.

If an orbit remains trapped for a long time, it will often follow a trajectory close to a boundary torus of the bubble (an outermost 2D torus). When such an orbit reaches the vicinity of P_+^l, it can be swept through the center of the bubble along the right branch of $W^u(P_+^l)$. This will lead to a return near P_+^r, and the orbit can repeat the process. A small number of trajectories make many turns inside the bubble becoming trapped for a long time near sticky, 2D tori. Each turn requires a passage close to the two saddle-foci where the orbit spends a relatively large number of iterates. The effect of repeated returns can be clearly seen in the trapping statistics plots of figure 5 especially for ε_1. Let us give some details on what is observed:

1. First, orbits that enter the bubble and leave it without being swept through the center, can escape more rapidly from $\mathcal{W}_+$ than those orbits that return close to P_+^r. This creates a discontinuity in the trapping statistics. The same thing happens for orbits that have multiple passages through the channel created by the 1D manifolds: for each additional passage there is a new discontinuity. Consequently, the trapping statistics in the figure show corresponding jumps (for, say, $10^3 \lessapprox t \lessapprox 10^4$ for ε_1).
2. Second, the relative measure of orbits that do not perform any close return to P_+^r decreases as the distance to the saddle-foci decreases. The implication is that there are more orbits spending shorter times near the bubble than longer times. For the statistics at ε_1, this explains the decrease in the abundance of trapped orbits for, say, $10^2 \lessapprox t \lessapprox 10^3$. Similar effects are seen, but to a smaller extent, for the orbits that pass multiple times through the channel. These effects are weaker, but still visible in the plots for ε_2 and ε_3.

As ε grows, the channel around the 1D manifolds that traps orbits grows in diameter, but can still play some role. For example, the slices for $\varepsilon = 1.0015$ in figure 6 show that some trapped orbits still can be stuck in a zone with larger volume near the 1D manifolds. Of course if ε is large enough this channel will be less important.

5.2. A transport model

A statistical model of transport usually assumes that ensembles evolve as a random walk on a discrete Markov chain with states corresponding to regions of phase space bounded by partial barriers. For area-preserving maps, the barriers are Cantori, and the transition flux between states is the turnstile area [36, 37, 40].

A simplified model for trapping statistics and anomalous diffusion corresponds to discretization into two such states [1, 30, 57, 60, 61]: a region $\mathcal{W} = \mathcal{W}_+ \cup \mathcal{W}_-$, (28), where orbits are accelerated, and its complement,

$$\mathcal{W}^c = \mathbb{T}^3 \setminus \mathcal{W}.$$

The idea is that when an orbit is in $\mathcal{W}$ it undergoes a *flight*, where the action grows linearly in time, and while it is in $\mathcal{W}^c$ it undergoes normal diffusion. In this model there are just two possible transitions: escape from, or entry into $\mathcal{W}$, i.e. the transitions $\mathcal{W} \to \mathcal{W}^c$ and $\mathcal{W}^c \to \mathcal{W}$, respectively. If we take $\mathcal{W}$ to be a vicinity of a bubble of stability, then this simplification requires that we know the exit-time probability $\mathcal{P}_\varepsilon(t)$ (29), the pdf of a $\mathcal{W} \to \mathcal{W}^c$ transition at time t. From our observations it seems plausible to assume that this has the power law form (6) with $b \in (2, 3)$. This is consistent with previous numerical results for a 3D map [48] and with

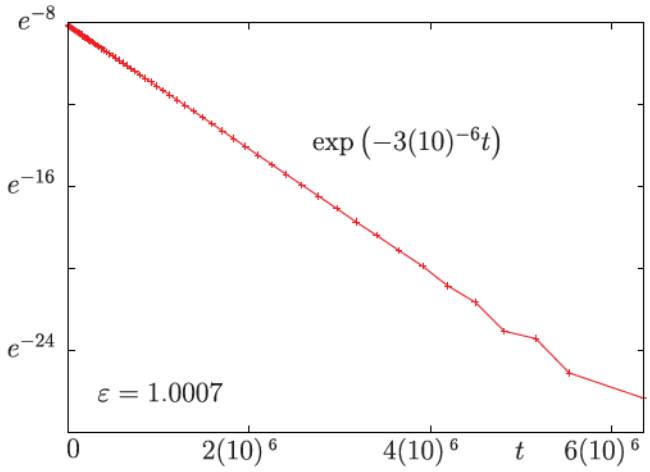

Figure 8. Exit time probability density function for $\mathcal{W}^c$ on a log-linear plot. The distribution is computed for $N = 2 \times 10^7$ initial conditions in a fundamental domain of the unstable manifold of the point $(3/4, 0, 0)$.

the observations for 2D maps, recall section 2.1. Note that b must be at least two since, when a map is volume preserving, Kac's theorem implies that the average exit time must exist [38]. When $b < 3$, the variance does not exist.

Of course the true distributions in figure 5 are not exactly power laws: there are jumps and oscillations. The former is probably due to low flux through regions containing newly broken tori, and the latter to the number of passages close to the saddle-foci $P^{r,l}_{\pm}$ [44, chapter 5].

The analogous pdf for the lengths of stays outside $\mathcal{W}$ is the exit-time distribution for $\mathcal{W}^c$. As was also observed in the area-preserving context [46], this distribution seems to be well approximated by an exponential. In figure 8 we show, for ε_1, the exit time distribution for $\mathcal{W}^c$ as a function of time. In essence, excluding fast returns to $\mathcal{W}$ (say, of length less than 50), it appears that the probability of entering $\mathcal{W}$ after spending t iterates in $\mathcal{W}^c$ seems to follow a geometric distribution with rate c, and hence that the exit time distribution for $\mathcal{W}^c$ is

$$\mathcal{P}(t) \sim (1-c)^t \sim \mathrm{e}^{-ct}, \tag{30}$$

when $c \ll 1$. Estimating c from a linear fit on a log-linear plot like figure 8 gives, for $\varepsilon_1, \varepsilon_2$, and ε_3,

$$c \approx 3.00 \times 10^{-6},\ 2.53 \times 10^{-6},\ \text{and}\ 2.10 \times 10^{-6},$$

respectively. Note that the average exit time is of the order of c^{-1} so that the average time in $\mathcal{W}^c$ is of the order of $4(10)^5$ iterates. That is, there are long periods outside the bubbles.

Correlations between the transitions $\mathcal{W} \to \mathcal{W}^c$ and $\mathcal{W}^c \to \mathcal{W}$ must be taken into account to be able to estimate the anomalous diffusion exponent χ from the trapping statistics. To measure these, we consider two random variables: say X, that denotes the length of a stay in $\mathcal{W}$; and Y, that measures the length of the next trapping segment in $\mathcal{W}^c$. In this way we can measure the correlation between successive stays in complementary regions.

For ε_1 and ε_2 we found that the correlation coefficient between X and Y to be small, i.e. to be inside the confidence interval at the level of 95% given by Student's t-test. However, for ε_3 we initially found correlations. This anomaly has an easy geometrical explanation: the shape of the bubble is increasingly distorted (by the cubic term in $\psi(z)$) as ε grows, recall figure 6.

The implication is that the size of the domain for $\mathcal{W}$ in (28) is too small to properly contain the trapped segments around the bubble. If we slightly increase the size of this domain to

$$\mathcal{W}_+ = \{(x, y, z) \ : \ |x| \leqslant 0.04, |y| \leqslant 0.15, |z| \leqslant 0.1\},$$

and an analogous form for $\mathcal{W}_-$, then the correlation between successive stays is again small. This enlargement only affects short stays in $\mathcal{W}$ and $\mathcal{W}^c$ due to orbits that are located on the periphery of the bubble. Hence, it has a minor effect on the long-time trapping statistics shown in figure 5 and the long-time behavior of σ_T shown in figure 4.

5.3. Relating anomalous diffusion to stickiness

Our numerical experiments suggest that the action diffusion for our map is anomalous, recall table 2. What is the relation between the exponent χ of σ_T and the exponent b of the exit time distribution? A number of previous studies of the analogous phenomena for 2D maps imply that

$$\chi = 2 - b/2, \tag{31}$$

see e.g. [24, 30, 31, 57, 60, 61]. However this result does not hold for our map when ε is close to one; the final column in table 2 shows the deviation of $\chi + b/2$ from the expected value of 2. Indeed, even the sign of the relation is not correct: as b increases, χ should decrease according to (31); instead it increases.

We believe that a major reason for this disagreement is the relatively small value of c in the exponential decay of the $\mathcal{W}^c \to \mathcal{W}$ transitions. The point is that even though we have iterated each initial condition up to 10^{11} times, we may still be far from observing the 'correct' asymptotic behavior. Indeed, the derivation of (31) relies on the $\mathcal{W}^c \to \mathcal{W}$ transitions being fast compared with those for $\mathcal{W} \to \mathcal{W}^c$. When c is small, orbits spend more time outside $\mathcal{W}$. Hence, for a fixed total number of iterates, less time is spent in $\mathcal{W}$. Thus longer experiments are probably needed to faithfully compute the effect of the $\mathcal{W} \to \mathcal{W}^c$ transitions on σ_T.

It would be interesting to take into account the role of the parameter c in the simple two-state transport model, especially to compute finite time corrections to an asymptotic exponent.

6. Conclusions

In the first part of this paper we constructed a family f_ε (13) of two-angle, one-action, volume-preserving maps of the cylinder $\mathbb{T}^2 \times \mathbb{R}$ that smoothly projects to the three-torus $\mathbb{T}^3$. This map has fixed point accelerator modes that are born whenever $\varepsilon = n$. The phase space of f_0 is foliated by horizontal, rotational invariant tori, and these persist when ε (and μ) is small according to volume-preserving versions of the KAM theorem. Thus our model generalizes Chirikov's standard map to the 3D volume-preserving setting.

The accelerator modes are created by a Hopf-one bifurcation. The local behavior near this bifurcation is modeled by the Michelson quadratic volume-preserving map (9). Previous studies of this map gave necessary conditions for the appearance of a bubble regular motion around the accelerator modes.

In the second part of the paper, we assessed the diffusive properties of the f_ε as ε varied near the first Hopf-one bifurction at $\varepsilon = 1$. We found, as expected, that if there are no accelerator modes, the action variable exhibits normal diffusive behavior: its standard deviation grows as $\sqrt{T}$. However when there is a bubble of stable orbits, the action diffusion seems to be anomalous: the standard deviation with exponent $\chi > 0.6$. Moreover, the exit time distribution

for a neighborhood of the bubble decay as a power-law t^{-b} with $b \in (2,3)$. Our experiments suggest that the distribution for the lengths of untrapped segments is exponential, and that stays outside and inside the bubbles are independent.

In this paper we provide evidence that $\mathcal{P}_\varepsilon(t) \sim t^{-b}$, $b \in (2,3)$, agreeing with the results in [48]. This contrasts with the exponential distribution for exit times observed for the map in [53]. We do not know the reason for this radical difference.

Another important question that remains is the relation between the exponents b and χ. From our computations, this differs from the relation obtained for the 2D case, recall section 5.3. We hypothesize that the reason for this is that the mean exit time from the complement of the bubbles is too long for our numerical experiments to reach their asymptotic limit.

The observed algebraic decay of the exit time distribution seems to imply that there exist remnants of destroyed invariant two-tori in the chaotic zone outside the KAM-bubble. These would be analogous to the Cantori for 2D twist maps. There is no theory, however, for the existence of these in the volume-preserving context. If one could find these remnants, and compute the flux through them, then it should be possible to construct a Markov tree model, similar to that in [42], that could explain the observed stickiness of the bubble. To solve these problems requires a theory for the destruction of invariant tori [23, 39]. Is there an analogue of Chirikov's overlap criterion? Are there remnant tori, and if so, what is their topology?

Acknowledgments

NM, CS, and AV were supported by grants MTM2016-80117-P (Spain) and 2017-SGR-1374 (Catalonia). JDM was supported by NSF grant DMS-1211350 (USA). We thank J Timoneda for maintaining the computing facilities of the Dynamical Systems Group of the Universitat de Barcelona, that have been largely used in this work. This work started while NM was visiting JDM at the University of Colorado Boulder under the scholarship EEBB-I-15-10119 (MINECO, Spain). Fruitful discussions with R Easton are also acknowledged.

Appendix A. A choice for $\psi(z)$

Here we construct a concrete example of an odd, degree-one circle map ψ that satisfies (14). This will be used in section 4 to give numerical evidence of anomalous diffusion in the dynamics of the map f_ε along the action variable.

First consider a function $\tilde{\psi}(z) = -z + c_3 z^3$ defined on $[0,1]$. If $c_3 \geqslant 4$ there is a unique $z_c \leqslant \frac{1}{2}$ such that $m_c = \tilde{\psi}'(z_c)$ is the slope of the straight line between $(z_c, \tilde{\psi}(z_c))$ and $(\frac{1}{2}, 0)$. The value z_c is determined as a solution of the cubic equation,

$$\tilde{\psi}'(z_c)(\frac{1}{2} - z_c) + \tilde{\psi}(z_c) = 0.$$

Define the C^1 function

$$\tilde{\psi}_{\text{ext}}(z) = \begin{cases} \tilde{\psi}(z) & \text{if} \quad z \in [0, z_c), \\ m_c(z - \frac{1}{2}) & \text{if} \quad z \in [z_c, 1 - z_c], \\ -\tilde{\psi}(1 - z) & \text{if} \quad z \in (1 - z_c, 1]. \end{cases}$$

This is an odd function with zero average. We will use an analytic approximation of it via (a truncated) Fourier series, that will only contain sine terms with coefficients $\hat{a}_k < 0$, and call

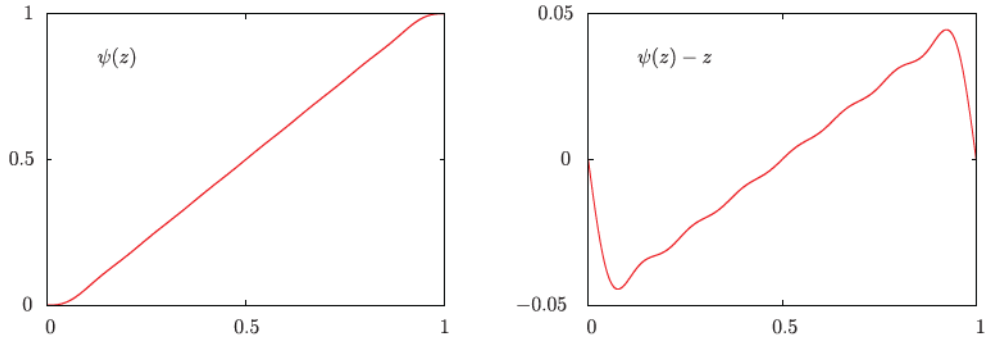

Figure A1. Left: function $\psi(z)$ in (13), see (15). Right: $\psi(z) - z$.

this approximation $\hat{\psi}_{\text{ext}}$. For the choice $c_3 = 8\pi^2$ it is enough to take the first seven harmonics to get a fairly good approximation of $\tilde{\psi}_{\text{ext}}$. That is, we take

$$\psi(z) = z + \lambda_c \hat{\psi}_{\text{ext}}(z) \approx z + \lambda_c \sum_{k=1}^{7} \hat{a}_k \sin(2\pi k z),$$

where $\lambda_c = |\mathrm{d}\hat{\psi}_{\text{ext}}(0)/dz|^{-1}$ is a correction factor to make sure that $\psi'(0) = 0$. For our map (13), this gives the form (15) with $a_i = \lambda_c \hat{a}_i$, $i = 1, \ldots, 7$ being

$$\begin{aligned} a_1 &= -0.031\,722\,552\,624\,100\,20, & a_5 &= -0.003\,946\,221\,282\,199\,23, \\ a_2 &= -0.015\,001\,446\,721\,045\,00, & a_6 &= -0.002\,573\,763\,696\,492\,51, \\ a_3 &= -0.009\,094\,902\,844\,667\,39, & a_7 &= -0.001\,599\,544\,834\,072\,87. \\ a_4 &= -0.005\,943\,571\,515\,810\,41, \end{aligned} \tag{A.1}$$

In figure A1 we can see the graph of $\psi(z)$ in $[0, 1]$ (left), and how much it differs from the identity (right).

Appendix B. Proof of lemma 1

Here we prove lemma 1, on the existence of fixed point accelerator modes for the map (13). Recall that the function $\psi(z)$ is assumed to be an odd, degree-one circle map that satisfies (14).

A point (x, y, z) belongs to an FPAM if $(x', y', z') = (x + n_1, y + n_2, z + n_3)$, $n_1, n_2, n_3 \in \mathbb{Z}$, and $n_3 \neq 0$. From (13) this implies

$$\mu \sin(2\pi y) + \psi(z') = n_1, \tag{B.1}$$

$$\nu \sin(2\pi z') = n_2, \tag{B.2}$$

$$\varepsilon\,(\cos(2\pi x) - \beta \sin(2\pi y)) = n_3. \tag{B.3}$$

Given the limits (17) and (B.2) implies that $n_2 = 0$, and thus either $z' = p$ or $z' = p + \frac{1}{2}$, for some $p \in \mathbb{Z}$.

1. Assume first that $z' = p \in \mathbb{Z}$. Since $z' - z = n_3$, then, $z = q = p - n_3 \in \mathbb{Z}$. Since $\psi(p) = p$, and μ is restricted by (17) and (B.1) requires that $n_1 = p$, which requires $y = y_\pm$ with $y_+ = r$ or $y_- = r + \frac{1}{2}$, for $r \in \mathbb{Z}$.

In particular, in both cases (B.3) reduces to $\varepsilon\cos(2\pi x) = n_3 \in \mathbb{Z}\setminus\{0\}$. Solutions to this equation are born at $\varepsilon = n_3$ at $x = s$ or $x = s + \frac{1}{2}$, being $s \in \mathbb{Z}$. Hence we have FPAM that are born when $\varepsilon = n_3$ at the points

$$P_+ = (0,0,0), \qquad Q_+ = (0,\frac{1}{2},0),$$
$$P_- = (\frac{1}{2},0,0), \qquad Q_- = (\frac{1}{2},\frac{1}{2},0),$$

on $\mathbb{T}^3$, and all equivalent lifts of these points to $\mathbb{R}^3$.
At the Hopf-one bifurcation, the linearization Df_ε should have 1 as eigenvalue. This holds since at the FPAM, $\cos(2\pi y_\pm) = \pm 1$ and $\sin(2\pi x) = 0$, and the first and second traces of Df_ε are

$$\tau = \sigma = 3 \mp 4\beta\varepsilon\pi^2\nu.$$

Finally, the second pair of multipliers is on the unit circle when $-1 < \tau = \sigma < 3$, which gives the requirement

$$0 < \pm\varepsilon\pi^2\beta\nu < 4.$$

Thus if $\beta\nu > 0$ only the fixed points $P_\pm$ have the stability property to become saddle-foci, recall remark 3.

2. If $z' = p + \frac{1}{2}$, $p \in \mathbb{Z}$, then since $\psi(z) - z$ is a period-one, odd function, $\psi(z') = \psi(p+\frac{1}{2}) = p + \psi(\frac{1}{2}) = p + \frac{1}{2}$. Thus (B.1) requires that $n_1 = p + \frac{1}{2} + \mu\sin(2\pi y) = 0$. Under the restriction (17), this implies that $n_1 \notin \mathbb{Z}$. Hence, no point in $\mathbb{T}^3$ of the form $P = (x, y, \frac{1}{2})$, $x, y \in \mathbb{S}^1$ can be an FPAM.

□

ORCID iDs

James D Meiss https://orcid.org/0000-0002-0019-0356
Narcís Miguel https://orcid.org/0000-0003-2745-1795
Carles Simó https://orcid.org/0000-0001-7350-3088
Arturo Vieiro https://orcid.org/0000-0003-2584-2717

References

[1] Altmann E G and Anomalous K H 2008 Transport in Hamiltonian systems *Anomalous Transport: Foundations, Applications* ed R Klages *et al* (New York: Wiley)
[2] Alus O, Fishman S and Meiss J D 2016 Probing the statistics of transport in the Hénon map *Eur. Phys. J.: Spec. Top.* **225** 1181–6
[3] Alus O, Fishman S and Meiss J D 2017 Universal exponent for transport in mixed hamiltonian dynamics *Phys. Rev.* E **96** 032204
[4] Bäcker A and Meiss J D 2018 Elliptic bubbles in Moser's 4D quadratic map: the quadfurcation *Nonlinearity* (submitted)
[5] Bäcker A and Meiss J D 2018 Moser's quadratic, symplectic map 2018 *Regular and Chaotic Dynamics* accepted (arXiv:1808.07229)
[6] Baldomá I, Castejón O and Seara T M 2013 Exponentially small heteroclinic breakdown in the generic Hopf-zero singularity *J. Dynam. Differ. Equ.* **25** 335–92
[7] Baldomá I, Castejón O and Seara T M 2018 Breakdown of a 2D heteroclinic connection in the Hopf-zero singularity (I) *J. Nonlinear Sci.* **28** 1551–627

[8] Baldomá I, Castejón O and Seara T M 2018 Breakdown of a 2D heteroclinic connection in the Hopf-zero singularity (II). The generic case *J. Nonlinear Sci.* **28** 1489–549

[9] Broer H, Simó C and Vitolo R 2008 Hopf saddle-node bifurcation for fixed points of 3D-diffeomorphisms: analysis of a resonance 'bubble' *Physica* D **237** 1773–99

[10] Broer H, Simó C and Vitolo R 2008 The Hopf-saddle-node bifurcation for fixed points of 3D-diffeomorphisms: the Arnol'd resonance web *Bull. Belg. Math. Soc. Simon Stevin* **15** 769–87

[11] Broer H W, Simó C and Vitolo R 2010 Chaos and quasi-periodicity in diffeomorphisms of the solid torus *Discrete Continuous Dyn. Syst.* B **14** 871–905

[12] Cheng C Q and Sun Y S 1989/90 Existence of invariant tori in three-dimensional measure-preserving mappings *Celest. Mech. Dynam. Astronom.* **47** 275–92

[13] Chirikov B V 1979 A universal instability of many-dimensional oscillator systems *Phys. Rep.* **52** 264–379

[14] Chirikov B V and Izraelev F M 1976 *Some Numerical Experiments with a Nonlinear Mapping: Stochastic Component (Transformations ponctuelles et leurs applications)* (Paris: Éditions Centre Nat. Recherche Sci.) pp 409–28

[15] Chirikov B V and Shepelyansky D L 1984 Correlation properties of dynamical chaos in Hamiltonian systems *Physica* D **13** 395–400

[16] Chirikov B V and Shepelyansky D L 1984 Statistics of Poincaré recurrences and the structure of a stochastic layer of nonlinear resonance *9th Int. Conf. on Nonlinear Oscillations (Kiev, 1981)* vol 2 (Kiev: Naukova Dumka) pp 421–4

[17] Contopoulos G and Harsoula M 2010 Stickiness effects in conservative systems *Int. J. Bifurcation Chaos Appl. Sci. Eng.* **20** 2005–43

[18] Cristadoro G and Ketzmerick R 2008 Universality of algebraic decays in Hamiltonian systems *Phys. Rev. Lett.* **100** 184101

[19] Dullin H R and Meiss J D 2008 Nilpotent normal form for divergence-free vector fields and volume-preserving maps *Physica* D **237** 156–66

[20] Dullin H R and Meiss J D 2009 Quadratic volume-preserving maps: invariant circles and bifurcations *SIAM J. Appl. Dyn. Syst.* **8** 76–128

[21] Dumortier F, Ibáñez S, Kokubu H and Simó C 2013 About the unfolding of a Hopf-zero singularity *Discrete Continuous Dyn. Syst.* **33** 4435–71

[22] Feingold M, Kadanoff L P and Piro O 1988 Passive scalars, three-dimensional volume-preserving maps and chaos *J. Stat. Phys.* **50** 529

[23] Fox A M and Meiss J D 2013 Greene's residue criterion for the breakup of invariant tori of volume-preserving maps *Physica* D **243** 45–63

[24] Geisel T, Zacherl A and Radons G 1988 Chaotic diffusion and 1/*f*-noise of particles in two-dimensional solids *Z. Phys.* B **71** 117–27

[25] Gonchenko S V, Meiss J D and Ovsyannikov I I 2006 Chaotic dynamics of three-dimensional Hénon maps that originate from a homoclinic bifurcation *Regul. Chaotic Dyn.* **11** 191–212

[26] Greene J M 1979 A method for determining a stochastic transition *J. Math. Phys.* **20** 1183–201

[27] Guckenheimer J and Kuznetsov Y A 2007 Fold–Hopf bifurcation *Scholarpedia* **2** 1855 (revision #91277)

[28] Hanson J D, Cary J and Meiss J D 1985 Algebraic decay in self-similar Markov chains *J. Stat. Phys.* **39** 327–45

[29] Holmes P 1984 Some remarks on chaotic particle paths in time-periodic, three-dimensional swirling flows *Fluids and Plasmas: Geometry and Dynamics (Boulder, Colo., 1983)* (*Contemporary Mathematics* vol 28) (Providence, RI: American Mathematical Society) pp 393–404

[30] Ishizaki R, Horita T, Kobayashi T and Mori H 1991 Anomalous diffusion due to accelerator modes in the standard map *Prog. Theor. Phys.* **85** 1013–22

[31] Karney C 1983 Long-time correlations in the stochastic regime *Physica* D **8** 360–80

[32] Karney C, Rechester A and White R 1981/82 Effect of noise on the standard mapping *Physica* D **4** 425–38

[33] Kook H T and Meiss J D 1990 Diffusion in symplectic maps *Phys. Rev.* A **41** 4143–50

[34] Lichtenberg A J and Lieberman M A 1992 *Regular and Chaotic Dynamics. Applied Mathematical Sciences* (New York: Springer)

[35] Lomelí H E and Meiss J D 1998 Quadratic volume-preserving maps *Nonlinearity* **11** 557–74

[36] MacKay R, Meiss J D and Percival I 1984 Transport in Hamiltonian systems *Physica* D **13** 55–81

[37] Meiss J D 1992 Symplectic maps, variational principles, and transport *Rev. Mod. Phys.* **64** 795–848

[38] Meiss J D 1997 Average exit time for volume-preserving maps *Chaos* **7** 139–47

[39] Meiss J D 2012 The destruction of tori in volume-preserving maps *Commun. Nonlinear Sci. Numer. Simul.* **17** 2108–21
[40] Meiss J D 2015 Thirty years of turnstiles and transport *Chaos* **25** 097602
[41] Meiss J D, Cary J R, Grebogi C, Crawford J D, Kaufman A N and Abarbanel H D I 1983 Correlations of periodic, area-preserving maps *Physica* D **6** 375–84
[42] Meiss J D and Ott E 1986 Markov tree model of transport in area-preserving maps *Physica* D **20** 387–402
[43] Michelson D 1986 Steady solutions of the Kuramoto–Sivashinsky equation *Physica* D **19** 89–111
[44] Miguel N 2016 Transport phenomena and anomalous diffusion in conservative systems of low dimension *PhD Thesis* Universitat de Barcelona
[45] Miguel N, Simó C and Vieiro A 2013 From the Hénon conservative map to the Chirikov standard map for large parameter values *Regul. Chaotic Dyn.* **18** 469–89
[46] Miguel N, Simó C and Vieiro A 2015 Effect of islands in diffusive properties of the standard map for large parameter values *Found. Comput. Math.* **15** 89–123
[47] Miles K, Nagarajan B and Zumbrunnen D 1995 Three-dimensional chaotic mixing of fluids in a cylindrical cavity *Trans. ASME: J. Fluids Eng.* **117** 582–8
[48] Mullowney P, Julien K and Meiss J D 2008 Chaotic advection and the emergence of tori in the Küppers–Lortz state *Chaos* **18** 033104
[49] Rechester A B, Rosenbluth M N and White R B 1981 Fourier-space paths applied to the calculation of diffusion for the Chirikov–Taylor model *Phys. Rev.* A **23** 2664–772
[50] Rom-Kedar V and Zaslavsky G 1999 Islands of accelerator modes and homoclinic tangles *Chaos* **9** 697–705
[51] Speetjens M, Clercx H and van Heijst G 2004 A numerical and experimental study on advection in three-dimensional Stokes flows *J. Fluid Mech.* **514** 77–105
[52] Sturman R, Meier S, Ottino J and Wiggins S 2008 Linked twist map formalism in two and three dimensions applied to mixing in tumbled granular flows *J. Fluid Mech.* **602** 129–74
[53] Sun Y S and Zhou L Y 2009 Stickiness in three-dimensional volume preserving mappings *Celest. Mech. Dynam. Astronom.* **103** 119–31
[54] Venegeroles R 2008 Calculation of superdiffusion for the Chirikov–Taylor model *Phys. Rev. Lett.* **101** 1–4
[55] Venegeroles R 2009 Universality of algebraic laws in Hamiltonian systems *Phys. Rev. Lett.* **102** 1–4
[56] Vitolo R, Broer H and Simó C 2010 Routes to chaos in the Hopf-saddle-node bifurcation for fixed points of 3D-diffeomorphisms *Nonlinearity* **23** 1919–47
[57] Weeks E R, Urbach J S and Swinney H L 1996 Anomalous diffusion in asymmetric random walks with a quasi-geostrophic flow example *Physica* D **97** 291–310
[58] Xia Z 1992 Existence of invariant tori in volume-preserving diffeomorphisms *Ergod. Theor. Dynam. Syst.* **12** 621–31
[59] Zaslavsky G M, Edelman M and Niyazov B A 1997 Self-similarity, renormalization, and phase space nonuniformity of Hamiltonian chaotic dynamics *Chaos* **7** 159–81
[60] Zumofen G and Klafter J 1993 Scale-invariant motion in intermittent chaotic systems *Phys. Rev.* E **47** 851–63
[61] Zumofen G and Klafter J 1994 Random walks in the standard map *Europhys. Lett.* **25** 585–70